SIMULATION OF PATCH ANTENNAS ON ARBITRARY DIELECTRIC SUBSTRATES - RWG BASIS FUNCTIONS

by

Anuja Apte

A Thesis submitted to the faculty of the

Worcester Polytechnic Institute

in partial fulfillment of the requirements for the

Degree of Master of Science

In Electrical and Computer Engineering

May 9th 2003

Approved by

Dr. Sergey Makarov **Dr. David Cyganski**

Dr. Marat Davidovitz **Dr. Brian King**

Abstract:

Based on the combined surface and volume RWG (Rao-Wilton-Glisson) basis functions, a simulator of a patch antenna on a finite dielectric substrate using the Method of Moments (MoM) has been implemented in Matlab. The metal surface is divided into planar triangular elements whereas the (inhomogeneous) dielectric volume is divided into tetrahedral elements.

The structure under study is comprised of a typical patch antenna consisting of a single patch above a finite ground plane, and a probe feed. The performance of the solver is studied for different mesh configurations.

The results obtained are tested by comparison with the commercial ANSOFT HFSS v8.5 and WIPL-D simulators. The former uses a large number of finite elements (up to 30,000) and adaptive mesh refinement, thus providing the reliable data for comparison.

Behavior of the most sensitive characteristic – antenna input impedance – is tested, close to the first resonant frequency. The error in the resonant frequency is estimated at different values of the relative dielectric constant ε_r, which ranges from 1 to 20. The reported results show reasonable agreement. However, the solver needs to be further improved.

Acknowledgements:

I would like to thank my adviser Prof. S. N. Makarov and the ECE Department of WPI for support of this work Special thanks to my best friend Shashank Kulkarni, who was of tremendous help for this research. At last but not at least, I wish to thank my parents for all good things they did for me.

Table of Contents:

List of Tables:

List of Symbols:

Symbol	Description
a_n	Area of face corresponding to the nth volume-RWG element
A_n^+	Area of plus triangle corresponding to the nth surface-RWG element
A_n^-	Area of minus triangle corresponding to the nth surface-RWG element
f_n^S	Basis function corresponding to the nth surface-RWG element
$\vec{f}_n^V$	Basis function corresponding to the nth volume-RWG element
l_n	Length of the nth surface-RWG element
m	Index for outer integral in a double integral
n	Index for inner integral in a double integral
$\vec{r}$	Position vector of observation point
$\vec{r}'$	Position vector of integration point
S	Metal Surface
t_n^+	Plus triangle corresponding to the nth surface-RWG element
t_n^-	Minus triangle corresponding to the nth surface-RWG element
T	Tetrahedral element of dielectric volume
T_n^+	Plus tetrahedron corresponding to the nth volume-RWG element
T_n^-	Minus tetrahedron corresponding to the nth volume-RWG element

List of Symbols (contd.):

Symbol	Description
V_n^+	Volume of plus tetrahedron corresponding to the nth volume-RWG element
V_n^-	Volume of minus tetrahedron corresponding to the nth volume-RWG element
$\vec{r}_n^{+S}$	Vector drawn from free vertex of triangle t_n^+ to the observation point
$\vec{r}_n^{-S}$	Vector drawn from observation point to the free vertex of triangle t_n^-
$\vec{r}_n^{+V}$	Vector drawn from free vertex of tetrahedron T_n^+ to the observation point
$\vec{r}_n^{-V}$	Vector drawn from observation point to the free vertex of tetrahedron T_n^-
Ω	Boundary of dielectric volume V

1. Introduction

1.1 Problem Statement

This thesis aims at simulation of combined metal-dielectric structures using the Method of Moments (MoM) based on surface-volume RWG (Rao-Wilton-Glisson) basis functions [1], [2]. A typical patch antenna structure consisting of a single patch above a finite ground plane was mostly considered in the present study. The performance of the solver (radiation/scattering) is studied for different mesh configurations and different dielectric constants of the substrate. Other straightforward applications of the present solver include simulation of antennas embedded in inhomogeneous dielectric (human body) and electromagnetic compatibility (EMC) problems of printed circuit boards designed for very high clock speeds.

1.2 Review of other simulation methods

Before going into the derivation and implementation of the MoM equations for the combined metal-dielectric structure, we summarize various approaches to simulate patch antennas and various software packages available for that purpose.

Finite Element Method (FEM): ANSOFT HFSS [3] is the commercially developed package for electromagnetic modeling. It uses the finite element method. The features of ANSOFT HFSS are

1. The geometric model is divided into large number of tetrahedra. The collection of these tetrahedra is referred as the finite element mesh.

2. HFSS uses FEM with the unknown vector quantities being volume electromagnetic fields and currents.
3. The FEM approach requires (sophisticated) absorbing boundary conditions at an artificial boundary.
4. As the structure is divided into larger number of tetrahedra for obtaining more accurate results and assuring internal convergence, the execution time becomes very high (from observations while working with ANSOFT HFSS).
5. ANSOFT HFSS can be used to model various inhomogeneous dielectric structures.

Method of Integral Equation (MIE) [4]: (surface to surface approach). WIPL-D [5] is another commercially available and relatively inexpensive package for electromagnetic modeling. It is based on the integral equation method, which implements the surface-to-surface approach – surface equivalence principle of electrodynamics. The integral equations for surface electric/magnetic currents are solved using the second-order basis functions. WIPL-D (WI stands for wires, PL stands for plates, and D stands for dielectrics) is a general-purpose 3D electromagnetic simulator in the frequency domain capable of handling any finite material bodies and also magnetic bodies. It is available in two versions, basic and professional. The basic version is limited to 350 unknowns for metallic structures and 500 unknowns for composite structures. It costs about $400. The most significant features of WIPL-D are the following:

1. The metallic and dielectric surfaces are modeled using quadrilateral patches.

2. The Method of Moments/Surface Integral Equation (SIE) code is used to compute the impedance matrix. In the MoM/SIE code the unknown quantities are surfaces currents (electric and magnetic). Hence, the number of unknowns and CPU time required by the MoM/SIE are usually much smaller than those of the FEM and MoM/VIE. Typical execution time per frequency step can be a fraction of second.
3. WIPL-D, being a MoM/SIE code, does not need any absorbing boundary conditions and associated discretization of the volume outside of the structure under investigation.
4. It does not allow modelling of inhomogeneous dielectric substrates and has noticeable problems with embedded metal objects. It doesn't allow considering periodic structures.

Integral equation method: (volume to surface approach [1, 2, 6]): This approach has been used in this thesis. It is based on the electric field integral equation (volume equivalence principle for the dielectric and surface equivalence principle for metal) and uses some basis/ testing functions for the derivation of MoM equations. The approach keeps the major advantage of FEM – capability with handling inhomogeneous dielectrics. At the same time, it doesn't need any absorbing boundary conditions. The approach is also readily extendable to the periodic case.

The system matrix is still dense, as it is typical for any MoM method. The structure of the system matrix will be discussed in the following sections. We suggest using combined surface-volume RWG basis functions [1, 2] to derive the system matrix. Such a choice is inviting for many reasons. The RWG basis functions are first-order vector-basis functions

that allow accurate representation of the field behavior. While the use of surface RWG basis functions is a well-known matter [7-10], the volume RWG basis functions are almost unknown. To the author's knowledge, this is the first use of combined RWG basis functions for modeling patch antennas.

1.3 RWG basis functions

Simulation of a combined metal-dielectric structure involves modeling of the metal surface and the dielectric volume, respectively. In this section we discuss the surface RWG basis functions used for modeling the metal surface [1] and then the volume RWG basis functions for modeling dielectric volume [2].

a. Definition

The metal surface is divided into triangular patches as shown in Fig.1.3.1.

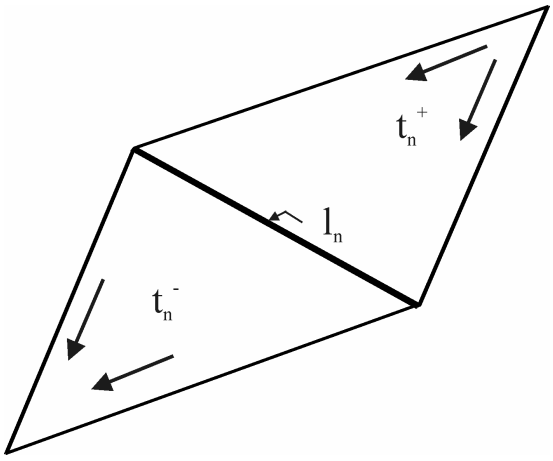

Fig.1.3.1 Surface RWG basis function

For any two triangular patches, t_n^+ and t_n^-, having areas A_n^+ and A_n^-, respectively, and sharing the common edge l_n, the n^{th} basis function is defined as

$$f_n^S(\vec{r}) = \begin{cases} \dfrac{l_n}{2A_n^+}\vec{r}_n^{+S} & \vec{r}\ in\ t_n^+ \\ \dfrac{l_n}{2A_n^-}\vec{r}_n^{-S} & \vec{r}\ in\ t_n^- \end{cases} \tag{1.3.1}$$

where $\vec{r}_n^{+S} = \vec{r} - \vec{r}_n^+$ is the vector drawn from free vertex of triangle t_n^+ to the observation point; $\vec{r}_n^{-S} = \vec{r}_n^- - \vec{r}$ is the vector drawn from the observation point to the free vertex of triangle t_n^-. The basis function is zero outside two adjacent triangles t_n^+ and t_n^-.

Volume RWG basis functions [2] are very similar to the surface RWG basis functions [1]. Instead of two adjacent triangular patches sharing the common edge, one needs to consider two adjacent tetrahedra sharing the common face as shown in Fig.1.3.2.

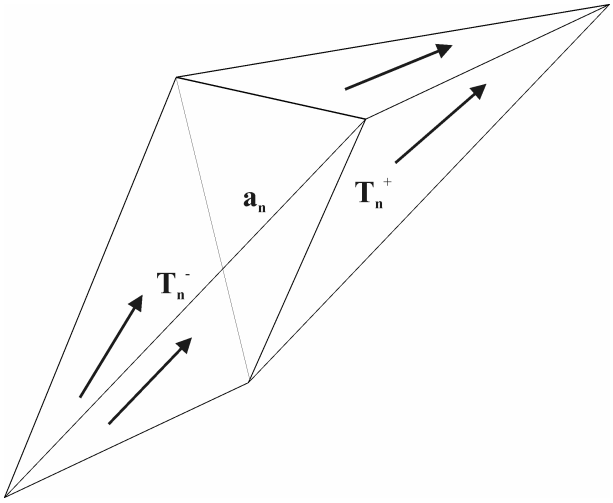

Fig.1.3.2 Volume RWG basis function

For any two tetrahedra, T_n^+ and T_n^-, having volumes V_n^+ and V_n^-, respectively, and sharing the common face a_n, the n^{th} basis function becomes

$$f_n^V(\vec{r}) = \begin{cases} \dfrac{a_n}{3V_n^+}\vec{r}_n^{+V} & \vec{r}\ in\ T_n^+ \\ \dfrac{a_n}{3V_n^-}\vec{r}_n^{-V} & \vec{r}\ in\ T_n^- \end{cases} \tag{1.3.2}$$

where $\vec{r}_n^{+V} = \vec{r} - \vec{r}_n^+$ is the vector drawn from free vertex of tetrahedron T_n^+ to the observation point; $\vec{r}_n^{-V} = \vec{r}_n^- - \vec{r}$ is the vector drawn from the observation point to the free vertex of tetrahedron T_n^-. The basis function is zero outside two adjacent tetrahedra T_n^+ and T_n^-.

The component of $\vec{f}_n^V$ normal to the n^{th} face is constant and continuous across the face because the normal component of $r_n^{\pm V}$ along face n is just the height of $T_n^\pm$ with face n as the base and the height expressed as $3V_n^\pm / a_n$. This latter factor normalizes $\vec{f}_n^V$ in (1.3.2) such that its flux density normal to face n is unity, ensuring continuity of the component of $\vec{f}_n^V$ normal to the face. Thus it can be showed that [2]

$$\vec{f}_n^V(\vec{r}) \cdot \hat{n} = 1 \quad \text{on face } n \tag{1.3.3}$$

Only one tetrahedron can be attached to the face, which lies on the boundary of the dielectric structure, say T_n^+. Therefore, the corresponding basis function is defined as in equation (1.3.2) but only within T_n^+. It is not defined otherwise [2].

b. Use

Since the volume RWG basis functions are used in conjunction with the volume equivalence principle [4] for a dielectric object, they must be able to support

i. Volume polarization currents

ii. Volume bound charges

iii. Surface bound charges.

The discussion of volume polarization currents and volume bound charges is straightforward [2]. It is therefore not duplicated here. However, the discussion of surface bound charges needs to be revisited.

The total electric flux density $\vec{D}(\vec{r})$ is expanded into a set of basis functions (1.3.2). Considering only one basis function for simplicity, one has

$$\vec{D}(\vec{r}) = D_n \vec{f}_n^V(\vec{r}) \tag{1.3.4}$$

The volume polarization current $\vec{J}_V(\vec{r})$, by definition [4], is given by

$$\vec{J}_V(\vec{r}) = jwK(\vec{r})\vec{D}(\vec{r}) \ , \tag{1.3.5}$$

where $K(\vec{r})$ is the contrast ratio,

$$K(\vec{r}) = \frac{\hat{e}(\vec{r}) - e_o}{\hat{e}(\vec{r})}$$

The total polarization charge is given by Gauss' theorem

$$jwr(\vec{r}) = -\nabla_V \cdot \vec{J}_V(\vec{r}) \tag{1.3.6}$$

which, after substitution of equation (1.3.5), becomes

$$r(\vec{r}) = -D_n K(\vec{r})\nabla_V \cdot \vec{f}_n^V - D_n \vec{f}_n^V(\vec{r})\nabla_V \cdot K \tag{1.3.7}$$

The first term on the right-hand side of equation (1.3.7) describes the volume bound charges. The second term is related to surface bound charges. This term appears when the permittivity and the contrast change abruptly. Thus, this term is formally represented by a generalized function (δ-function).

Below, we will check the behavior of bound surface charges

$$r_S(\vec{r}) = -D_n \vec{f}_n^V(\vec{r})\nabla_V \cdot K \tag{1.3.8}$$

for different physical situations.

c. Types of dielectric boundary

Consider three cases depicted in Fig. 1.3.3. In the first case (a), the "full" volume RWG element lies within the (inhomogeneous) dielectric. It includes two tetrahedra with piecewise constant dielectric contrasts, i.e.

$$K^+ = const, \quad K^- = const \tag{1.3.9}$$

respectively. In the second case (b), the "boundary" volume RWG element lies on the boundary dielectric-air. It has the constant contrast

$$K^+ = const \tag{1.3.10}$$

almost everywhere within T_n^+ but not on the face a_n. This last remark actually assures the presence of surface bound charges on the boundary. If the gradient of the contrast would be absent, the volume RWG basis functions wouldn't be able to support surface boundary charges on the boundary dielectric – air. Finally, in the third case (c), the "boundary" volume RWG element lies on the boundary dielectric-metal. It again has the constant contrast

$$K^+ = const \tag{1.3.11}$$

almost everywhere within T_n^+ but not on the face a_n.

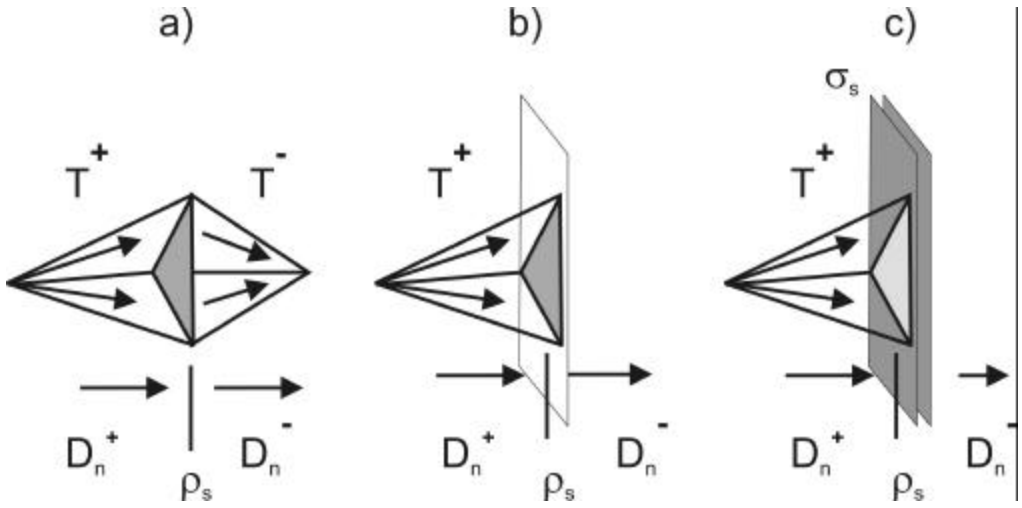

Fig.1.3.3 Surface bound charges supported by a volume RWG basis function.

d. Surface bound charges – inner face between two different dielectrics

In case (a) of Fig.1.3.3 it follows from equations (1.3.8) and (1.3.3) that

$$r_S(\vec{r}) = -D_n \vec{f}_n^{\,V}(\vec{r})\nabla_V \cdot K = -D_n \lim_{h\to 0} \frac{K^- - K^+}{h} \qquad (1.3.12a)$$

since $\vec{f}_n^{\,V}(\vec{r}) \cdot \hat{n} = 1$ on face n and the direction of the normal vector is from left to right in Fig. 1. Equation (1.3.12a) leads to the residing surface charge density

$$r_S(\vec{r}) = -D_n(K^- - K^+) = D_n(K^+ - K^-) = D_n^+(K^+ - K^-) = D_n^-(K^+ - K^-) \qquad (1.3.12b)$$

On the other hand, it is well known that "the bound charge density at the interface between two dielectrics 1 and 2 is

$$r_S(\vec{r}) = (\vec{P}_1 - \vec{P}_2) \cdot \hat{n} \tag{1.3.12c}$$

where the polarization in 1 is $\vec{P}_1$ and is directed *into* the interface; the polarization in 2 is $\vec{P}_2$ and points *away* from the interface" [11]. By definition

$$\vec{P}(\vec{r}) = K(\vec{r})\vec{D}(\vec{r}) \tag{1.3.12d}$$

We plug (1.3.12d) in (1.3.12c) to obtain equation (1.3.12b). *Thus, the volume RWG basis functions exactly satisfy the boundary condition at the dielectric-dielectric interface*. Indeed, the total electric flux is continuous across the face, i.e. $D_n^+ = D_n^-$ [11].

e. Surface bound charges – boundary face at air-dielectric interface

In this case we must assume equation (1.3.10) to hold almost everywhere within T_n^+. On the face itself, the contrast K^- must become zero, which corresponds to the case of air. Then,

$$r_S(\vec{r}) = -D_n \vec{f}_n^V(\vec{r}) \nabla_V \cdot K = -D_n \lim_{h \to 0} \frac{0 - K^+}{h} \tag{1.3.13a}$$

and

$$r_S(\vec{r}) = D_n^+ K^+ \qquad (1.3.13b)$$

which is the particular case of the result of previous section. We can conclude that the boundary condition is also satisfied at the boundary between the dielectric and air.

f. Surface bound charges – boundary face at dielectric-metal interface

In this case we must assume equation (1.3.11) to hold almost everywhere within T_n^+. On the face itself, the contrast will have some value K^-, which is a priori unknown. Let's try to find that value, using the boundary condition at the metal-dielectric interface. One has [11] (Fig.1.3.3c)

$$r_S(\vec{r}) = \left(\frac{1}{e_R} - 1\right) s_S; \quad s_S = -D_n^+ \qquad (1.3.14a)$$

where s_S is the free charge density on the *contact* side of the metal interface. It follows from equation (1.3.14a) that

$$r_S(\vec{r}) = \left(\frac{e_R - 1}{e_R}\right) D_n^+ = K^+ D_n^+ \qquad (1.3.14b)$$

On the other hand, when the dielectric contrast drops down to some value K^- on the face itself, the surface charge is going to be (1.3.12b)

$$r_S(\vec{r}) = D_n^+(K^+ - K^-) \tag{1.3.14c}$$

Comparing equations (1.3.14b) and (1.3.14c) one sees that it should be

$$K^- = 0 \tag{1.3.14d}$$

in order to be consistent with the boundary conditions on the dielectric-metal interface.

g. Point of concern

On the one hand, the condition

$$K^- = 0 \tag{1.3.15}$$

corresponds to the boundary face in contact with air. On the other hand, it corresponds to the boundary face in contact with metal (cf. previous section). It seems that we cannot discriminate between those two conditions a *priori*, which leads to the following paradox. Any boundary face in contact with metal must satisfy equation (1.3.15). Thus, it can be treated as a face in contact with air as well. Therefore, it should be an air gap between the metal and the dielectric of infinitesimally small thickness. Such an air gap is dangerous since it usually assumes very high fields and significant parasitic impedance.

To eliminate this uncertainty, one can introduce the boundary condition between metal and dielectric explicitly. In other words, one should put

$$s_S = -D_n^+ \tag{1.3.16}$$

into MoM equations explicitly. While the boundary condition is implemented in the elegant way when the metal face is in contact with dielectric, i.e.

$$s^{total}{}_S = -D_n^+ + D_n^- \tag{1.3.17}$$

for the total surface charge density $s^{total}{}_S$ on the metal surface, it is difficult to implement it for the infinitely thin metal sheet on the boundary dielectric-air.

With this discussion as a background of RWG basis functions, we will pursue the derivation of Method of Moment (MoM) equations for a simple patch antenna structure in the following section.

2. Derivation of MoM equations

In this section the MoM equations is derived for a pure metallic, a pure dielectric and a combined metal-dielectric structure based on the surface-volume RWG basis functions. The derivations in this section form the core of the solver, which is tested in the following section.

2.1 MoM equations for a metallic (air-filled) patch antenna

In this section, the MoM equation for a pure metal object (an antenna or a scatterer) is accurately derived for the electric field integral equation (EFIE) [4], utilizing RWG basis functions [1].

a. Scattering problem

The total electric field (antenna or scattering problem) is a combination of the incident field (labeled by superscript *i*) and the scattered field (labeled by superscript *s*), i.e.

$$\vec{E} = \vec{E}^{\,i} + \vec{E}^{\,s} \tag{2.1.1}$$

The incident field is either the incoming signal (scattering problem) or the excitation electric field in the antenna feed (radiation problem). The scattered field has a

straightforward interpretation for the scattering problem. For the antenna radiation, the "scattered" field is just the field radiated by the antenna.

The scattered electric field $\vec{E}^s$ is due to surface currents and free charges on the metal surface *S* (the so-called mixed-potential formulation)

$$\vec{E}^s = -jw\vec{A}_S(\vec{r}) - \nabla\Phi_S(\vec{r}) \quad \vec{r} \text{ on } S \tag{2.1.2}$$

The magnetic vector potential $\vec{A}_S(\vec{r})$ describes current radiation whereas the electric potential $\Phi_S(\vec{r})$ describes charge radiation. In the near field, the Φ-contribution is somewhat more critical than the $\vec{A}$-contribution. In the far-field, the Φ-contribution is negligibly small. On the metal surface *S*, the tangential component of the electric field, $\vec{E}_{\tan} = 0$, thus giving the EFIE,

$$E^i_{\tan} = \left(jw\vec{A}_S + \nabla\Phi_S\right)_{\tan} \quad \vec{r} \text{ on } S \tag{2.1.3}$$

b. Test functions

Assume that some test functions, $\vec{f}^S_m(\vec{r})$ $m = 1 \ldots N_M$, cover the entire surface *S* and do not have a component normal to the surface. Multiplication of (2.1.3) by $\vec{f}^S_m$ and integration over *S* gives N_M equations

$$\int_S \vec{f}_m^S \cdot \vec{E}^i d\vec{r} = jw \int_S \vec{f}_m^S \cdot \vec{A}_S d\vec{r} - \int_S \left(\nabla \cdot \vec{f}_m^S\right) \Phi_S d\vec{r} \tag{2.1.4}$$

since

$$\int_S \nabla \Phi_S \cdot \vec{f}_m^S d\vec{r} = -\int_S \Phi_S \nabla_S \cdot \vec{f}_m^S d\vec{r} \tag{2.1.5}$$

if $\vec{f}_m^S$ doesn't have a component perpendicular to the surface boundary or edge (if any).

c. Surface current/charge expansions

The surface current density, $\vec{J}_S$ is expanded into basis function (which usually coincide with the test functions) in the form

$$\vec{J}_S = \sum_{n=1}^{N_M} I_n \vec{f}_n^S \tag{2.1.6}$$

The magnetic vector potential [1]

$$\vec{A}_S(\vec{r}) = \frac{m}{4p} \int_S \vec{J}_S g d\vec{r}' \tag{2.1.7}$$

after substitution of expansion (2.1.6) becomes

$$\vec{A}_S(\vec{r}) = \sum_{n=1}^{N_M} \left\{ \frac{m}{4p} \int_S \vec{f}_n^S(\vec{r}') g d\vec{r}' \right\} I_n \tag{2.1.8}$$

where $g = \exp(-jkR)/R, R = |\vec{r} - \vec{r}'|$ is the free-space Green's function (time dependency $\exp(jwt)$ is assumed everywhere). Similarly, the electric potential,

$$\Phi_S(\vec{r}) = \frac{1}{4pe} \int_S s_S g dr', \quad jw s_S = -\nabla_S \cdot J \tag{2.1.9}$$

(s_s is the surface charge density) has the following form

$$\Phi_S(\vec{r}) = \sum_{n=1}^{N_M} \left\{ \frac{1}{4pe} \frac{j}{w} \int_S \nabla_S \cdot f_n^S(\vec{r}') d\vec{r}' \right\} I_n \tag{2.1.10}$$

d. Moment equations

The moment equations are obtained if we substitute expansions (2.1.8) and (2.1.10) into the primary equation (2.1.4). In terms of symbolic notations,

$$u_m = \sum_{n=1}^{N_M} Z_{mn}^{MM} I_n, \quad m = 1,..., N_M \tag{2.1.11}$$

where

$$u_m = \int_S \vec{f}_m^{\,S} \cdot \vec{E}^{\,i} d\vec{r} \qquad (2.1.12)$$

are the "voltage" or excitation components for every test/basis function and

$$Z_{mn}^{MM} = \left(\frac{jwm}{4p}\right) \int_S \int_S \vec{f}_m^{\,S}(\vec{r}) \cdot \vec{f}_n^{\,S}(\vec{r}\,') g d\vec{r}\,' d\vec{r} - \left(\frac{j}{4pwe}\right) \int_S \int_S \left(\nabla_S \cdot \vec{f}_m^{\,S}\right)\left(\nabla_S \cdot \vec{f}_n^{\,S}\right) g d\vec{r}\,' d\vec{r} \qquad (2.1.13)$$

are the components of the impedance matrix of the size (N_M x N_M). Note that the impedance matrix is symmetric for any set of basis functions (test functions should be the same) when the corresponding surface integrals are calculated precisely. The components of the impedance matrix are the double surface integrals of the Green's function and they mostly reflect the geometry of the problem. In the matrix form, (2.1.11) becomes

$$\vec{u} = \hat{Z}\vec{I} \qquad (2.1.14)$$

e. RWG basis functions

Below, we recall the following properties of the RWG basis functions [1]. For any two triangular patches, t_n^+ and t_n^-, having areas A_n^+ and A_n^-, and sharing the common edge l_n, the n-th basis function becomes

$$f_n^S(\vec{r}) = \begin{cases} \dfrac{l_n}{2A_n^+}\,\vec{r}_n^{+S} & \vec{r}\ in\ t_n^+ \\ \dfrac{l_n}{2A_n^-}\,\vec{r}_n^{-S} & \vec{r}\ in\ t_n^- \end{cases} \tag{2.1.15}$$

and

$$\nabla_S \cdot f_n^S(\vec{r}) = \begin{cases} \dfrac{l_n}{A_n^+} & \vec{r}\ in\ t_n^+ \\ -\dfrac{l_n}{A_n^-} & \vec{r}\ in\ t_n^- \end{cases} \tag{2.1.16}$$

where $\vec{r}_n^{+S} = \vec{r} - \vec{r}_n^+$ is the vector drawn from free vertex of triangle t_n^+ to the observation point; $\vec{r}_n^{-S} = \vec{r}_n^- - \vec{r}$ is the vector drawn from the observation point to the free vertex of triangle t_n^-. The basis function is zero outside two adjacent triangles t_n^+ and t_n^-.

Substitution of equations (2.1.15), (2.1.16) into equation (2.1.13) gives the components of the impedance matrix in terms of surface RWG basis functions in the form

$$\begin{aligned} &\int_S\int_S \vec{f}_m^S \cdot \vec{f}_n^S\, g d\vec{r}\,' d\vec{r} = \\ &+\frac{l_m l_n}{4A_m^+A_n^+}\int_{t_m^+}\int_{t_n^+}\left(\vec{r}_m^{+S}\cdot\vec{r}_n'^{+S}\right)g d\vec{r}\,' d\vec{r} + \frac{l_m l_n}{4A_m^+A_n^-}\int_{t_m^+}\int_{t_n^-}\left(\vec{r}_m^{+S}\cdot\vec{r}_n'^{-S}\right)g d\vec{r}\,' d\vec{r} \\ &+\frac{l_m l_n}{4A_m^-A_n^+}\int_{t_m^-}\int_{t_n^+}\left(\vec{r}_m^{-S}\cdot\vec{r}_n'^{+S}\right)g d\vec{r}\,' d\vec{r} + \frac{l_m l_n}{4A_m^-A_n^-}\int_{t_m^-}\int_{t_n^-}\left(\vec{r}_m^{-S}\cdot\vec{r}_n'^{-S}\right)g d\vec{r}\,' d\vec{r} \end{aligned} \tag{2.1.17}$$

and

$$\int_S\int_S \nabla_S \cdot \vec{f}_m^{\,S} \nabla_S \cdot \vec{f}_n^{\,S} g d\vec{r}' d\vec{r} =$$
$$+\frac{l_m l_n}{A_m^+ A_n^+}\int_{t_m^+}\int_{t_n^+} g d\vec{r}' d\vec{r} - \frac{l_m l_n}{A_m^+ A_n^-}\int_{t_m^+}\int_{t_n^-} g d\vec{r}' d\vec{r} \qquad (2.1.18)$$
$$-\frac{l_m l_n}{A_m^- A_n^+}\int_{t_m^-}\int_{t_n^+} g d\vec{r}' d\vec{r} + \frac{l_m l_n}{A_m^- A_n^-}\int_{t_m^-}\int_{t_n^-} g d\vec{r}' d\vec{r}$$

f. Integral calculation

Calculation of the surface integrals presented in equations (2.1.17), (2.1.18) forms a major part (about 90%) in the evaluation of the MoM impedance matrix for RWG basis functions. Consider a structure where all triangular patches are enumerated by $p = 1,..., P$. Then, every integral in equation (2.1.17) is build upon the term

$$\vec{A}_{S\,pq}^{ij} = \int_{t_p}\int_{t_q} \left(\vec{r}_i^{\,S} \cdot \vec{r}'^{\,S}_j\right) g(|\vec{r} - \vec{r}'|) d\vec{r}' d\vec{r} \quad p, q = 1,..., P \quad i, j = 1,2,3 \qquad (2.1.19)$$

Here, $\vec{r}_i^{\,S} = \vec{r} - \vec{r}_i$ for any vertex *i* of patch *p* whereas $\vec{r}'^{\,S}_j = \vec{r}' - \vec{r}_j$ for any vertex *j* of patch *q*. Similarly, every integral in equation (2.1.18) is build upon the term

$$\Phi_{S\,pq} = \int_{t_p}\int_{t_q} g(|\vec{r} - \vec{r}'|) d\vec{r}' d\vec{r} \quad p, q = 1,..., P \qquad (2.1.20)$$

The integrals (2.1.19) and (2.1.20) can be found using a vectorized routine, which employs Gaussian integration of variable order (up to 7th) for both the surface integrals [12, 13].

Calculation is performed over all triangular patches, not over RWG basis functions. The corresponding formulas are given in Appendix B.

g. Self-integrals

The self-integrals ($p = q$ in equations (2.1.19), (2.1.20)) are found precisely, using a number of analytical base integrals presented in [14]. Before doing that, the Taylor expansion is written for the Green's function

$$g = \exp(-jkR)/R \approx 1/R - jk - \frac{k^2 R}{2} ... \tag{2.1.21}$$

Therefore

$$\Phi_{Spp} = \int_{t_p}\int_{t_p} g(|\vec{r} - \vec{r}'|)d\vec{r}'d\vec{r} \approx \int_{t_p}\int_{t_p} \frac{1}{|\vec{r} - \vec{r}'|} d\vec{r}'d\vec{r} - jkA_p^2 \quad p = 1,...,P \tag{2.1.22}$$

and

$$A_{Spp}^{ij} \approx \int_{T_p}\int_{T_p} \frac{(\vec{r} - \vec{r}_i)\cdot(\vec{r}' - \vec{r}_j)}{|\vec{r} - \vec{r}'|} d\vec{r}'d\vec{r} - jk\int_{T_p}\int_{T_p} (\vec{r} - \vec{r}_i)\cdot(\vec{r}' - \vec{r}_j)d\vec{r}'d\vec{r} \tag{2.1.23}$$
$$p = 1,...,P \quad i, j = 1,2,3$$

Introduction of the simplex coordinates l_1, l_2 for the triangle t_p gives [14]

$$\vec{r} = l_1(\vec{r}_1 - \vec{r}_3) + l_2(\vec{r}_2 - \vec{r}_3) + \vec{r}_3, \quad \vec{r}\,' = l_1'(\vec{r}_1 - \vec{r}_3) + l_2'(\vec{r}_2 - \vec{r}_3) + \vec{r}_3 \tag{2.1.24}$$

and

$$\begin{aligned}
&(\vec{r} - \vec{r}_i)\cdot(\vec{r}\,' - \vec{r}_j) = \\
&\quad (\vec{r}_3 - \vec{r}_i)\cdot(\vec{r}_3 - \vec{r}_j)\times 1 + \\
&\quad (\vec{r}_1 - \vec{r}_3)\cdot(2\vec{r}_3 - \vec{r}_i - \vec{r}_j)\times l_1 + \\
&\quad (\vec{r}_2 - \vec{r}_3)\cdot(2\vec{r}_3 - \vec{r}_i - \vec{r}_j)\times l_2 + \\
&\quad (\vec{r}_1 - \vec{r}_3)\cdot(\vec{r}_1 - \vec{r}_3)\times l_1 l_1' + \\
&\quad (\vec{r}_2 - \vec{r}_3)\cdot(\vec{r}_2 - \vec{r}_3)\times l_2 l_2' + \\
&\quad (\vec{r}_1 - \vec{r}_3)\cdot(\vec{r}_2 - \vec{r}_3)\times l_1 l_2' + \\
&\quad (\vec{r}_1 - \vec{r}_3)\cdot(\vec{r}_2 - \vec{r}_3)\times l_1' l_2
\end{aligned} \tag{2.1.25}$$

Substitution of equation (2.1.25) into the first term on the right-hand side of equation (2.1.23) results in seven integrals. Each of those is reduced to one of the four independent base integrals given in [14]. The remaining values are obtained using cyclic transformation. Integral (2.1.22) only needs the first base integral [14]. The second term on the right-hand side of equation (2.1.23) is calculated straightforwardly. Further details are given in Appendix B.

h. Impedance matrix filling –batch method

After the integrals (2.1.19) and (2.1.20) are calculated and stored, the complete impedance matrix is found by substitution of (2.1.17) and (2.1.18) into equation (2.1.13) and using equations (2.1.19), (2.1.20), in the form

$$Z_{mn}^{MM} =$$

$$+\frac{j}{4pwe} l_m l_n \begin{Bmatrix} +\frac{1}{A_m^+ A_n^+} \Phi_{S\,p(m^+)q(n^+)} & -\frac{1}{A_m^+ A_n^-} \Phi_{S\,p(m^+)q(n^-)} \\ -\frac{1}{A_m^- A_n^+} \Phi_{S\,p(m^-)q(n^+)} & +\frac{1}{A_m^- A_n^-} \Phi_{S\,p(m^-)q(n^-)} \end{Bmatrix}$$

$$-\frac{jwm}{16p} l_m l_n \begin{Bmatrix} +\frac{1}{A_m^+ A_n^+} A_{S\,p(m^+)q(n^+)}^{i(m^+)j(n^+)} & -\frac{1}{A_m^+ A_n^-} A_{S\,p(m^+)q(n^-)}^{i(m^+)j(n^-)} \\ -\frac{1}{A_m^- A_n^+} A_{S\,p(m^-)q(n^+)}^{i(m^-)j(n^+)} & +\frac{1}{A_m^- A_n^-} A_{S\,p(m^-)q(n^-)}^{i(m^-)j(n^-)} \end{Bmatrix} \tag{2.1.26}$$

Here, $p(m^{\pm})$ is the patch number corresponding either to plus or minus triangle of the RWG basic function m, respectively. Indexes $q(n^{\pm})$ have a similar meaning.

Index $i(m^{\pm})$ is the vertex number of the triangular patch, corresponding to the free vertex of either plus or minus triangle of the RWG basic function m, respectively. Indexes $j(n^{\pm})$ have a similar meaning.

Switching between plus and minus sign in the second part on the right-hand side of equation (2.1.26) is due to the opposite sign of $\vec{r}_n^{+S}$ and $\vec{r}_n^{-S}$. In equation (2.1.20), only "positive" $\vec{r}$ (or $\vec{r}^{+S}$) were formally considered. To include $\vec{r}^{-S}$ into consideration one therefore needs to change the sign of the corresponding term.

The impedance matrix $\hat{Z}$ can be filled using two nested loops over the total number of RWG basis functions. This procedure doesn't imply possible double calculations of the same surface integrals (cf. discussion in [1]). The reason is that all the surface integral pairs

(2.1.19) and (2.1.20) were already found for different triangular patches on the previous step.

Although the batch filling is very fast, it requires a substantial amount of RAM and cannot typically be used when the size of the impedance matrix exceeds 5,000x5,000. Therefore, one can utilize another method, where only one row of the impedance matrix is calculated at a time.

2.2 MoM equation for a pure dielectric structure

In this section, the MoM equation for a purely dielectric object (a scatterer) is accurately derived from the electric field integral equation (EFIE) [4], utilizing volume RWG basis functions [2].

a. Scattering problem

The total electric field (antenna or scattering problem) in a dielectric volume is a combination of the incident field (labeled by superscript *i*) and the scattered field (labeled by superscript *s*), i.e.

$$\vec{E} = \vec{E}^{\,i} + \vec{E}^{\,s} \tag{2.2.1}$$

Let V denote the volume of a lossy, inhomogeneous, dielectric body with (complex) dielectric constant $\hat{e}(\vec{r}) = e(\vec{r}) - js(\vec{r})/w$, where e and s are the medium permittivity and conductivity when $\vec{r}$ is in V. The total electric field in that case can be expressed in terms of the electric flux density, $\vec{D}(\vec{r})$ as

$$\vec{E} = \vec{D}(\vec{r})/\hat{e}(\vec{r})$$

The incident field is the incoming signal for the scattering problem. The scattered electric field $\vec{E}^s$ is found using the volume equivalence principle [4]. The dielectric material is removed and replaced by equivalent volume polarization currents. The scattered field is due to volume polarization currents in dielectric volume V (bounded by surface Ω) as follows

$$\vec{E}^s = -jw\vec{A}_V(\vec{r}) - \nabla\Phi_V(\vec{r}) \quad \vec{r} \text{ in } V \tag{2.2.2}$$

The magnetic vector potential $\vec{A}_V(\vec{r})$ describes radiation of volume polarization currents, whereas the electric potential $\Phi_V(\vec{r})$ describes radiation of the associated bound charges. In the far field, the Φ-contribution is negligibly small. Thus, from the expressions for $\vec{E}$ and $\vec{E}^s$, we can write the EFIE as

$$\vec{E}^i = \frac{\vec{D}(\vec{r})}{\hat{e}(\vec{r})} + jw\vec{A}_V(\vec{r}) + \nabla\Phi_V(\vec{r}) \quad \vec{r} \text{ in } V \tag{2.2.3}$$

b. Test functions

Assume that some test functions, $\vec{f}_m^{\,V}(\vec{r})$ $m = 1\ldots N_D$, cover the entire dielectric volume V. Multiplication of equation (2.2.3) by $\vec{f}_m^{\,V}(\vec{r})$ and integration over volume V gives N_D equations

$$\int_V \vec{f}_m^{\,V}(\vec{r})\cdot\vec{E}^i d\vec{r} = \int_V \frac{\vec{D}(\vec{r})}{\hat{e}(\vec{r})}\cdot\vec{f}_m^{\,V}(\vec{r})d\vec{r} + jw\int_V \vec{f}_m^{\,V}(\vec{r})\cdot\vec{A}_V d\vec{r} - \int_V \Phi_V\left(\nabla\cdot\vec{f}_m^{\,V}(\vec{r})\right)d\vec{r} + \int_\Omega \Phi_V\left(\vec{f}_m^{\,V}(\vec{r})\cdot\hat{n}\right)d\vec{r} \tag{2.2.4}$$

since

$$\int_V \nabla\Phi_V\cdot\vec{f}_m^{\,V}(\vec{r}) = -\int_V \Phi_V\left(\nabla\cdot\vec{f}_m^{\,V}(\vec{r})\right)d\vec{r} + \int_\Omega \Phi_V\left(\hat{n}\cdot\vec{f}_m^{\,V}(\vec{r})\right)d\vec{r}$$

where Ω is the boundary of V or the boundary of a region where $\vec{f}_m^{\,V}(\vec{r})$ is defined, and $\hat{n}$ is the outer unit normal to the surface Ω.

c. Volume current/charge expansions

The volume polarization current $\vec{J}_V(\vec{r})$, by definition, is written in terms of the electric flux density $\vec{D}(\vec{r})$ [2] in the form

$$\vec{J}_V(\vec{r}) = jwK(\vec{r})\vec{D}(\vec{r}) \ , \tag{2.2.5}$$

where $K(\vec{r})$ is the contrast ratio,

$$K(\vec{r}) = \frac{\hat{e}(\vec{r}) - e_o}{\hat{e}(\vec{r})}$$

The electric flux density $\vec{D}(\vec{r})$ is expanded into a set of basis functions (which usually coincide with the test functions) as

$$\vec{D}(\vec{r}) = \sum_{n=1}^{N_D} D_n \vec{f}_n^V(\vec{r}) \tag{2.2.6}$$

The volume current density, $\vec{J}_V(\vec{r})$ can be expanded in the form

$$\vec{J}_V(\vec{r}) = jw \sum_{n=1}^{N_D} D_n K_n(\vec{r}) \vec{f}_n^V(\vec{r}) \tag{2.2.7}$$

Thus, the magnetic vector potential [2]

$$\vec{A}_V(\vec{r}) = \frac{m}{4p} \int_V \vec{J}_V(\vec{r}\,') g d\vec{r}\,' \tag{2.2.8}$$

after substitution of expansion (2.2.7) becomes

$$\vec{A}_V(\vec{r}) = \left(\frac{jwm}{4p}\right)\sum_{n=1}^{N_D}\left\{\int_V K_n(\vec{r}')\,\vec{f}_n^{\,V}(\vec{r}')gd\vec{r}'\right\}D_n \tag{2.2.9}$$

where $g = \exp(-jkR)/R$, $R = |\vec{r} - \vec{r}'|$ is the free-space Green's function (time dependency $\exp(jwt)$ is assumed everywhere). Similarly, the electric potential (r is the volume charge density[1])

$$\Phi_V(\vec{r}) = \left(\frac{1}{4pe}\right)\int_V r(\vec{r}')gd\vec{r}', \quad jwr(\vec{r}) = -\nabla_V \cdot \vec{J}_V(\vec{r}) \tag{2.2.10}$$

has the following form

$$\Phi_V(\vec{r}) = \left(\frac{1}{4pe}\right)\sum_{n=1}^{N_D}\left\{\int_V K_n(\vec{r}')\left(\nabla \cdot \vec{f}_n^{\,V}(\vec{r}')\right)gd\vec{r}' + \int_V \left(\nabla K_n(\vec{r}')\right)\vec{f}_n^{\,V}(\vec{r}')gd\vec{r}'\right\}D_n \tag{2.2.11}$$

The first term on the right-hand side of equation (2.2.3) can be expanded in the form

$$\frac{\vec{D}(\vec{r})}{\hat{e}(\vec{r})} = \sum_{n=1}^{N_D}\left(\frac{1}{\hat{e}_n(\vec{r})}\right)D_n\,\vec{f}_n^{\,V}(\vec{r}) \tag{2.2.12}$$

[1] The volume charge density in homogeneous dielectric is zero, except for bound (surface) charges.

d. Moment equations

The moment equations are obtained if we substitute expansions (2.2.9), (2.2.11) and (2.2.12) into the primary equation (2.2.4). In terms of symbolic notations,

$$u_m = \sum_{n=1}^{N_D} Z_{mn}^{DD} D_n \tag{2.2.13}$$

where

$$u_m = \int_u \vec{f}_m(\vec{r}) \cdot \vec{E}^i d\vec{r} \tag{2.2.14}$$

are the "voltage" or excitation components for every test/basis function and

$$Z_{mn}^{DD} = \left[\begin{array}{l} \dfrac{-w^2 m}{4p} \displaystyle\int_V \int_V \vec{f}_m^{\,V}(\vec{r}) \cdot \vec{f}_n^{\,V}(\vec{r}\,') K_n g d\vec{r}\,' d\vec{r} \\ -\dfrac{1}{4pe} \left\{ \begin{array}{l} \displaystyle\int_V \int_V \left(\nabla \cdot \vec{f}_m^{\,V}(\vec{r})\right)\left(\nabla \cdot \vec{f}_n^{\,V}(\vec{r}\,')\right) K_n g d\vec{r}\,' d\vec{r} + \int_V \int_V \left(\nabla \cdot \vec{f}_m^{\,V}(\vec{r})\right) \vec{f}_n^{\,V}(r') \left(\nabla K_n(\vec{r}\,')\right) g d\vec{r}\,' d\vec{r} \\ -\displaystyle\int_\Omega \int_V \left(\vec{f}_m^{\,V}(\vec{r}) \cdot \hat{n}\right)\left(\nabla \cdot \vec{f}_n^{\,V}(\vec{r}\,')\right) K_n g d\vec{r}\,' d\vec{r} - \int_\Omega \int_V \left(\vec{f}_m^{\,V}(\vec{r}) \cdot \hat{n}\right) \vec{f}_n^{\,V}(\vec{r}\,') \left(\nabla K_n(\vec{r}\,')\right) g d\vec{r}\,' d\vec{r} \end{array} \right\} \\ + \displaystyle\int_V \frac{1}{\hat{e}(\vec{r}\,')} \vec{f}_m^{\,V}(\vec{r}) \cdot \vec{f}_n^{\,V}(\vec{r}\,') d\vec{r} \end{array} \right] \tag{2.2.15}$$

are the components of the impedance matrix of the size N_D x N_D. Note that the impedance matrix is symmetric for any set of basis functions (test functions should be the same) when the corresponding volume integrals are calculated precisely. The components of the

impedance matrix are the double volume and/or surface integrals of the Green's function and they mostly reflect the geometry of the problem. In the matrix form, equation (2.2.13) becomes

$$\vec{u} = \hat{Z}\vec{D} \tag{2.2.16}$$

e. RWG basis functions

Below, we recall the following properties of the volume RWG basis functions [2]. For any two tetrahedra, T_n^+ and T_n^-, having volumes V_n^+ and V_n^-, and sharing the common face a_n, the *n*-th basis function becomes

$$f_n^V(\vec{r}) = \begin{cases} \dfrac{a_n}{3V_n^+}\vec{r}_n^{+V} & \vec{r}\ in\ T_n^+ \\ \dfrac{a_n}{3V_n^-}\vec{r}_n^{-V} & \vec{r}\ in\ T_n^- \end{cases} \tag{2.2.17}$$

and

$$\nabla_V \cdot f_n^V(\vec{r}) = \begin{cases} \dfrac{a_n}{V_n^+} & \vec{r}\ in\ T_n^+ \\ -\dfrac{a_n}{V_n^-} & \vec{r}\ in\ T_n^- \end{cases} \tag{2.2.18}$$

where $\vec{r}_n^{+V} = \vec{r} - \vec{r}_n^{+}$ is the vector drawn from free vertex of tetrahedron T_n^+ to the observation point; $\vec{r}_n^{-V} = \vec{r}_n^{-} - \vec{r}$ is the vector drawn from the observation point to the free vertex of tetrahedron T_n^-. The basis function is zero outside two adjacent tetrahedra T_n^+ and T_n^-.

The component of $\vec{f}_n^V$ normal to the n^{th} face is constant and continuous across the face because the normal component of $r_n^{\pm V}$ along face n is just the height of $T_n^{\pm}$ with face n as the base and the height expressed as $3V_n^{\pm}/a_n$. This latter factor normalizes $\vec{f}_n^V$ in (2.2.17) such that its flux density normal to face n is unity, ensuring continuity of the component of $\vec{f}_n^V$ normal to the face. Thus it can be showed that [2]

$$\vec{f}_n^V(\vec{r}) \cdot \hat{n} = 1 \quad \text{on face } n \tag{2.2.19}$$

Consider the second term on the right-hand side of equation (2.2.11) given as,

$$\int_V \left(\nabla K_n(\vec{r}')\right) \vec{f}_n^V(\vec{r}') g d\vec{r}' \tag{2.2.20}$$

The term $\left(\nabla K_n(\vec{r}')\right)$ is zero if the n^{th} face is separating two identical dielectrics. But if the n^{th} face is separating two dissimilar media, different contrast ratios will be associated with two tetrahedra sharing the n^{th} face. Thus,

$$\left(\nabla K_n(\vec{r}\,')\right) = \left(K_n^+ - K_n^-\right) d(s)\ \hat{n}$$

where K_n^+ and K_n^- are the contrast ratios associated with T_n^+ and T_n^- sharing the n^{th} face, respectively, and $d(s)$ is the surface delta-function. This allows us to express the volume integral (2.2.20) in the form

$$\int_V \left(\nabla K_n(\vec{r}\,')\right) \vec{f}_n^{\,V}(\vec{r}\,')\, g d\vec{r}\,' = \left(K_n^+ - K_n^-\right) \int_{S_n} g d\vec{r}\,' \tag{2.2.21}$$

Substitution of equations (2.2.17), (2.2.18) into equation (2.2.15) and substitutions of equations (2.2.19) and (2.2.21) give the components of the impedance matrix in terms of volume RWG basis functions. Hereafter we have assumed that contrast K is constant within each tetrahedron. So that $K_n(\vec{r})$ can be represented as just K_n for n^{th} tetrahedron. Following similar procedure for $\hat{e}(\vec{r})$, the expressions for the integrals in (2.2.15) can be written in the form

$$\begin{aligned}
&\int_V \int_V \vec{f}_m^{\,V}(\vec{r}) \cdot \vec{f}_n^{\,V}(\vec{r}\,') g d\vec{r}\,' d\vec{r} = \\
&+ \frac{a_m a_n K_n^+}{9 V_m^+ V_n^+} \int_{T_m^+} \int_{T_n^+} \left(\vec{r}_m^{\,+V}(\vec{r}) \cdot \vec{r}_n^{\,+V}(\vec{r}\,')\right) g d\vec{r}\,' d\vec{r} + \frac{a_m a_n K_n^-}{9 V_m^+ V_n^-} \int_{T_m^+} \int_{T_n^-} \left(\vec{r}_m^{\,+V}(\vec{r}) \cdot \vec{r}_n^{\,-V}(\vec{r}\,')\right) g d\vec{r}\,' d\vec{r} \\
&+ \frac{a_m a_n K_n^+}{9 V_m^- V_n^+} \int_{T_m^-} \int_{T_n^+} \left(\vec{r}_m^{\,-V}(\vec{r}) \cdot \vec{r}_n^{\,+V}(\vec{r}\,')\right) g d\vec{r}\,' d\vec{r} + \frac{a_m a_n K_n^-}{9 V_m^- V_n^-} \int_{T_m^-} \int_{T_n^-} \left(\vec{r}_m^{\,-V}(\vec{r}) \cdot \vec{r}_n^{\,-V}(\vec{r}\,')\right) g d\vec{r}\,' d\vec{r}
\end{aligned} \tag{2.2.22}$$

$$\int_V\int_V \nabla\cdot\vec{f}_m^{\,V}(\vec{r})\nabla\cdot\vec{f}_n^{\,V}(\vec{r}\,')g d\vec{r}\,' d\vec{r} =$$
$$+\frac{a_m a_n K_n^+}{V_m^+ V_n^+}\int_{T_m^+}\int_{T_n^+} g d\vec{r}\,' d\vec{r} - \frac{a_m a_n K_n^-}{V_m^+ V_n^-}\int_{T_m^+}\int_{T_n^-} g d\vec{r}\,' d\vec{r} \qquad (2.2.23)$$
$$-\frac{a_m a_n K_n^+}{V_m^- V_n^+}\int_{T_m^-}\int_{T_n^+} g d\vec{r}\,' d\vec{r} + \frac{a_m a_n K_n^-}{V_m^- V_n^-}\int_{T_m^-}\int_{T_n^-} g d\vec{r}\,' d\vec{r}$$

$$\int_V\int_\Omega \left(\nabla\cdot\vec{f}_m^{\,V}(\vec{r})\right)\left(\nabla K_n(\vec{r}\,')\right) g d\vec{r}\,' d\vec{r} = \int_V\int_{S_n} \left(\nabla\cdot\vec{f}_m^{\,V}(\vec{r})\right)\left(\nabla K_n(\vec{r}\,')\right) g d\vec{r}\,' d\vec{r}$$
$$= \frac{\left(K_n^+ - K_n^-\right)a_m}{V_m^+}\int_{T_m^+}\int_{S_n} g d\vec{r}\,' d\vec{r} - \frac{\left(K_n^+ - K_n^-\right)a_m}{V_m^-}\int_{T_m^+}\int_{S_n} g d\vec{r}\,' d\vec{r} \qquad (2.2.24)$$

$$\int_\Omega\int_V \left(\nabla\cdot\vec{f}_n^{\,V}(\vec{r}\,')\right) K_n(\vec{r}\,') g d\vec{r}\,' d\vec{r} = \frac{K_n^+ a_n}{V_n^+}\int_{S_m}\int_{T_n^+} g d\vec{r}\,' d\vec{r} - \frac{K_n^- a_n}{V_n^-}\int_{S_m}\int_{T_n^+} g d\vec{r}\,' d\vec{r} \qquad (2.2.25)$$

$$\int_{S_m}\int_{S_n} \left(\nabla K_n(\vec{r}\,')\right) g d\vec{r}\,' d\vec{r} = \left(K_n^+ - K_n^-\right)\int_{S_m}\int_{S_n} g d\vec{r}\,' d\vec{r} \qquad (2.2.26)$$

and

$$\int_V \frac{1}{\hat{e}(\vec{r}\,')}\vec{f}_m^{\,V}(\vec{r})\cdot\vec{f}_n^{\,V}(\vec{r}\,') d\vec{r}$$
$$= \left[\begin{array}{l} \dfrac{1}{\hat{e}_m}\dfrac{a_m a_n}{9V_m^+ V_n^+}\displaystyle\int_{T_m^+}\left(\vec{r}_m^{\,+V}\cdot\vec{r}_n^{\,+V}\right) g d\vec{r} + \dfrac{1}{\hat{e}_m}\dfrac{a_m a_n}{9V_m^+ V_n^-}\displaystyle\int_{T_m^+}\left(\vec{r}_m^{\,+V}\cdot\vec{r}_n^{\,-V}\right) g d\vec{r} \\ + \dfrac{1}{\hat{e}_m}\dfrac{a_m a_n}{9V_m^- V_n^+}\displaystyle\int_{T_m^+}\left(\vec{r}_m^{\,-V}\cdot\vec{r}_n^{\,+V}\right) g d\vec{r} + \dfrac{1}{\hat{e}_m}\dfrac{a_m a_n}{9V_m^- V_n^-}\displaystyle\int_{T_m^+}\left(\vec{r}_m^{\,-V}\cdot\vec{r}_n^{\,-V}\right) g d\vec{r} \end{array}\right] \qquad (2.2.27)$$

f. Integral calculation

Evaluation of the MoM impedance matrix for RWG basis functions is by 90% the calculation of the volume/volume; volume/surface and surface/surface integrals presented in equations (2.2.22) to (2.2.27). Consider a structure where all tetrahedral volumes are enumerated by $p = 1,...,P$. Then, every integral in equation (2.2.22) is built upon the term

$$A_{Vpq}^{ij} = \int_{T_p}\int_{T_q} \left(\vec{r}_i^{\,V} \cdot \vec{r}\,'^{\,V}_j\right) g(|\vec{r} - \vec{r}\,'|) d\vec{r}\,' d\vec{r} \quad p,q = 1,...,P \quad i,j = 1,2,3,4 \tag{2.2.28}$$

Also, every integral in equation (2.2.23) is built upon the term

$$\Phi_{Vpq}^{1} = \int_{T_p}\int_{T_q} g(|\vec{r} - \vec{r}\,'|) d\vec{r}\,' d\vec{r} \quad p,q = 1,...,P \tag{2.2.29}$$

Every integral in equation (2.2.24) is built upon the term

$$\Phi_{Vpq}^{2} = \int_{T_p}\int_{S_q} g(|\vec{r} - \vec{r}\,'|) d\vec{r}\,' d\vec{r} \quad p,q = 1,...,P \tag{2.2.30}$$

Every integral in equation (2.2.25) is built upon the term

$$\Phi_{Vpq}^{3} = \int_{S_p}\int_{T_q} g(|\vec{r} - \vec{r}\,'|) d\vec{r}\,' d\vec{r} \quad p,q = 1,...,P \tag{2.2.31}$$

Every integral in equation (2.2.26) is built upon the term

$$\Phi^4_{Vpq} = \int_{S_p}\int_{S_q} g(|\vec{r} - \vec{r}'|)d\vec{r}'d\vec{r} \quad p,q = 1,...,P \tag{2.2.32}$$

Similarly, every integral in equation (2.2.27) is built upon the term

$$D^{ij}_{Vp} = \int_{T_p} \left(\vec{r}_i^{\,V} \cdot \vec{r}'^{\,V}_j\right) g(|\vec{r} - \vec{r}'|)d\vec{r}'d\vec{r} \quad p,q = 1,...,P \quad i,j = 1,2,3 \tag{2.2.33}$$

Here, $\vec{r}_i^{\,V} = \vec{r} - \vec{r}_i'$ for any vertex *i* of tetrahedron *p* whereas $\vec{r}'^{\,V}_j = \vec{r}' - \vec{r}_j'$ for any vertex *j* of tetrahedron *q*. The integrals (2.2.28)-(2.2.33) are found using a vectorized routine, which employs Gaussian integration of variable order (up to 10^{th}) for both the volume integrals [13], [15]. Calculation is performed over all tetrahedral patches, not over RWG basis functions. The corresponding formulas are given in Appendix B.

2.3 MoM equations for a combined metal-dielectric structure

In this section, the MoM equations for a combined metal-dielectric object (a scatterer) are accurately derived for the electric field integral equation (EFIE) [4], utilizing surface and volume RWG basis functions [1], [2] following the approach as given in [6].

a. Scattering problem

The total electric field (scattering problem) is combination of the incident field (labeled by superscript *i*) and the scattered field (labeled by superscript *s*), i.e.

$$\vec{E} = \vec{E}^{\,i} + \vec{E}^{\,s} \tag{2.3.1}$$

Let V denote the volume of a lossy, inhomogeneous, dielectric body with (complex) dielectric constant $\hat{e}(\vec{r}) = e(\vec{r}) - js(\vec{r})/w$, where e and s are the medium permittivity and conductivity when $\vec{r}$ is in V. Let a metal surface *S* be attached to this dielectric object. The incident field is the incoming signal for the scattering problem. The scattered electric field $\vec{E}^{\,s}$ in this case will have two components. One is due to volume polarization currents

$$\vec{J}_V(r) = jw(\hat{e}(r) - e_o)\vec{E}(r) \tag{2.3.2}$$

in the dielectric volume V and associated bound charges on the boundaries of an inhomogeneous dielectric region, and the other component is due to surface currents and free charges on the metal surface *S*. Using the expressions for scattered field in terms of electric and magnetic potentials $\vec{A}$ and Φ one has

$$\vec{E}^{\,s} = -jw\vec{A}_V(\vec{r}) - \nabla\Phi_V(\vec{r}) - jw\vec{A}_S(\vec{r}) - \nabla\Phi_S(\vec{r}) \quad \vec{r} \text{ in } V \tag{2.3.3a}$$

$$\vec{E}^{\,s} = -jw\vec{A}_S(\vec{r}) - \nabla\Phi_S(\vec{r}) - jw\vec{A}_V(\vec{r}) - \nabla\Phi_V(\vec{r}) \quad \vec{r} \text{ on } S \tag{2.3.3b}$$

where index V refers to dielectric volume and index S refers to metal surface, respectively. The magnetic vector potential $\vec{A}(\vec{r})$ and electric potential $\Phi(\vec{r})$ carry their usual meanings corresponding to metal and dielectric. Since

$\vec{D} = \hat{e}\vec{E}$, in the dielectric volume V (2.3.4a)

$\vec{E}_{\tan} = 0$, on the metal surface S (2.3.4b)

using the expressions for $\vec{E}$ and $\vec{E}^s$, we can write the EFIE as

$$\vec{E}^i = \frac{\vec{D}(\vec{r})}{\hat{e}(\vec{r})} + jw\vec{A}_V(\vec{r}) + \nabla\Phi_V(\vec{r}) + jw\vec{A}_S(\vec{r}) + \nabla\Phi_S(\vec{r}) \quad \vec{r} \text{ in } V \tag{2.3.5a}$$

$$\vec{E}^i_{\tan} = \left[+ jw\vec{A}_S(\vec{r}) + \nabla\Phi_S(\vec{r}) + jw\vec{A}_V(\vec{r}) + \nabla\Phi_V(\vec{r}) \right]_{\tan} \quad \vec{r} \text{ on } S \tag{2.3.5b}$$

b. Test functions

Assume that the volume test functions, $\vec{f}_m^V(\vec{r})$ m = 1… N_D, cover the entire dielectric volume V. Each function is defined (different from zero) within a smaller volume V_m. Multiplication of equation (2.3.5a) by $\vec{f}_m^V(\vec{r})$ and integration over volume V gives N_D equations

$$\int_V \vec{f}_m^{\,V}(\vec{r}) \cdot \vec{E}^i d\vec{r} = \left[\begin{array}{l} \underbrace{\int_{V_m} \vec{f}_m^{\,V}(\vec{r}) \frac{\vec{D}(\vec{r})}{\hat{e}(\vec{r})} d\vec{r} + jw \int_{V_m} \vec{f}_m^{\,V}(\vec{r}) \cdot \vec{A}_V d\vec{r} - \int_{V_m} \left(\nabla \cdot \vec{f}_m^{\,V}(\vec{r})\right) \Phi_V d\vec{r} + \int_{\Omega_m} \left(\hat{n}(\vec{r}) \cdot \vec{f}_m^{\,V}(\vec{r})\right) \Phi_V d\vec{r}}_{Z^{DD}} \\ \underbrace{+ jw \int_{V_m} \vec{f}_m^{\,V}(\vec{r}) \cdot \vec{A}_S d\vec{r} - \int_{V_m} \left(\nabla \cdot \vec{f}_m^{\,V}(\vec{r})\right) \Phi_S d\vec{r} + \int_{\Omega_m} \left(\hat{n}(\vec{r}) \cdot \vec{f}_m^{\,V}(\vec{r})\right) \Phi_S d\vec{r}}_{Z^{MD}} \end{array} \right] \tag{2.3.6}$$

since

$$\int_{V_m} \vec{f}_m^{\,V}(\vec{r}) \cdot \nabla \Phi_{V,S} d\vec{r} = -\int_{V_m} \Phi_{V,S} \left(\nabla \cdot \vec{f}_m^{\,V}(\vec{r})\right) d\vec{r} + \int_{\Omega_m} \Phi_{V,S} \left(\hat{n}(\vec{r}) \cdot \vec{f}_m^{\,V}(\vec{r})\right) d\vec{r} \tag{2.3.7}$$

where Ω_m is the boundary of volume V_m and $\hat{n}$ is the unit outer normal to the surface Ω_m bounding volume V_m. Note that Ω_m and S may intersect. The term on the right-hand side of equation (2.3.6), labeled Z^{DD}, is exactly the right-hand side of equation (2.2.4) from section 2.2 for pure dielectric. The term, labeled Z^{MD}, describes the contribution of radiation from the metal surface to the dielectric volume.

Now assume that the surface test functions, $\vec{f}_m^{\,S}(\vec{r})$ m = 1… N_M, cover the entire metal surface S and do not have a component normal to the surface. Each function is defined (different from zero) within a smaller surface S_m. Multiplication of equation (2.3.5b) by $\vec{f}_m^{\,S}(\vec{r})$ and integration over surface S gives N_M equations

$$\int_S \vec{f}_m^{\,S}(\vec{r}) \cdot \vec{E}^i \, d\vec{r} = \begin{bmatrix} \underbrace{+ jw \int_{S_m} \vec{f}_m^{\,S}(\vec{r}) \cdot \vec{A}_S \, d\vec{r} - \int_{S_m} \left(\nabla \cdot \vec{f}_m^{\,S}(\vec{r})\right) \Phi_S \, d\vec{r}}_{Z^{MM}} \\ \\ \underbrace{+ jw \int_{S_m} \vec{f}_m^{\,S}(\vec{r}) \cdot \vec{A}_V \, d\vec{r} - \int_{S_m} \left(\nabla \cdot \vec{f}_m^{\,S}(\vec{r})\right) \Phi_V \, d\vec{r}}_{Z^{DM}} \end{bmatrix} \tag{2.3.8}$$

since

$$\int_{S_m} \vec{f}_m^{\,S}(\vec{r}) \cdot \nabla \Phi_{V,S} \, d\vec{r} = - \int_{S_m} \Phi_{V,S} \left(\nabla \cdot \vec{f}_m^{\,S}(\vec{r})\right) d\vec{r} \tag{2.3.9}$$

The term on the right-hand side of equation (2.3.8), labeled Z^{MM}, is exactly the right-hand side of equation (2.1.4) from section 2.1 for pure metal. The term, labeled Z^{DM}, describes the contribution of radiation from the dielectric volume to the metal surface.

c. Surface, Volume current/charge expansions

Here we recall the equations for expansion of magnetic vector potential and electric potentials in terms of the corresponding basis functions.

The surface current density, $\vec{J}_S$ for the metal surface, is expanded into N_M surface RWG basis functions $\vec{f}_n^{\,S}$ in the form (identical to section 2.1)

$$\vec{J}_S = \sum_{n=1}^{N_M} I_n \vec{f}_n^{\,S} \tag{2.3.10}$$

The magnetic vector potential [1] after substitution of expansion (2.3.10) becomes

$$\vec{A}_S(\vec{r}) = \sum_{n=1}^{N_M} \left\{ \frac{m}{4p} \int_S \vec{f}_n^{\,S}(\vec{r}\,') g d\vec{r}\,' \right\} I_n \tag{2.2.11}$$

Where $g = \exp(-jkR)/R$, $R = \left|\vec{r} - \vec{r}\,'\right|$ is the free-space Green's function (time dependency $\exp(jwt)$ is assumed everywhere). Similarly, the electric potential takes the form, (identical to section 2.1)

$$\Phi_S(\vec{r}) = \frac{1}{4pe} \sum_{n=1}^{N_M} \left\{ \frac{j}{w} \int_S \nabla \cdot f_n^{\,S}(\vec{r}\,') g d\vec{r}\,' \right\} I_n \tag{2.3.12}$$

Turning to dielectric, the volume polarization current $\vec{J}_V(\vec{r})$ is written in terms of the electric flux density $\vec{D}(\vec{r})$ [2]

$$\vec{J}_V(\vec{r}) = jwK(\vec{r})\vec{D}(\vec{r}) \ , \tag{2.3.13}$$

where $K(\vec{r})$ is the contrast ratio

$$K(\vec{r}) = \frac{\hat{e}(\vec{r}) - e_o}{\hat{e}(\vec{r})} \tag{2.3.14}$$

The electric flux density $\vec{D}(\vec{r})$ is expanded into a set of basis functions ($m = 1 \ldots N_D$,) as

$$\vec{D}(\vec{r}) = \sum_{n=1}^{N_D} D_n \vec{f}_n^V(\vec{r}) \tag{2.3.15}$$

The volume current density, $\vec{J}_V(\vec{r})$ can be expanded in the form

$$\vec{J}_V(\vec{r}) = jw \sum_{n=1}^{N_D} D_n K_n(\vec{r}) \vec{f}_n^V(\vec{r}) \tag{2.3.16}$$

Thus, the magnetic vector potential [2]

$$\vec{A}_V(\vec{r}) = \frac{m}{4p} \int_V \vec{J}_V(\vec{r}') g d\vec{r}' \tag{2.3.17}$$

after substitution of expansion (2.3.7) becomes

$$\vec{A}_V(\vec{r}) = \left(\frac{jwm}{4p} \right) \sum_{n=1}^{N_D} \left\{ \int_V K_n(\vec{r}') \vec{f}_n^V(\vec{r}') g d\vec{r}' \right\} D_n \tag{2.3.18}$$

where $g = \exp(-jkR)/R$, $R = |\vec{r} - \vec{r}'|$ is the free-space Green's function (time dependency $\exp(jwt)$ is assumed everywhere). Similarly, the electric potential (r is the volume charge density)

$$\Phi_V(\vec{r}) = \left(\frac{1}{4pe}\right)\int_V r(\vec{r}')gd\vec{r}', \quad jwr(\vec{r}) = -\nabla\cdot\vec{J}_V(\vec{r}) \tag{2.3.19}$$

has the following form

$$\Phi_V(\vec{r}) = \left(\frac{1}{4pe}\right)\sum_{n=1}^{N_D}\left\{\int_V K_n(\vec{r}')\left(\nabla\cdot\vec{f}_n^{\,V}(\vec{r}')\right)gd\vec{r}' + \int_V\left(\nabla\cdot K_n(\vec{r}')\right)\vec{f}_n^{\,V}(\vec{r}')gd\vec{r}'\right\}D_n \tag{2.3.20}$$

The first term on the right-hand side of equation (2.3.5a) can be expanded in the form

$$\frac{\vec{D}(\vec{r})}{\hat{e}(\vec{r})} = \sum_{n=1}^{N_D}\left(\frac{1}{\hat{e}_n(\vec{r})}\right)D_n\vec{f}_n^{\,V}(\vec{r}) \tag{2.3.21}$$

d. Moment equations

The moment equations are obtained if we substitute expansions (2.3.11), (2.3.12) and (2.3.18), (2.3.20), (2.3.21) into equations (2.3.6), (2.3.8). In terms of symbolic notations,

$$u_m^{\,V} = \sum_{n=1}^{N_D} Z_{mn}^{DD}D_n + \sum_{n=1}^{N_M} Z_{mn}^{MD}I_n \tag{2.3.22a}$$

$$u_m^{\,S} = \sum_{n=1}^{N_M} Z_{mn}^{MM}I_n + \sum_{n=1}^{N_D} Z_{mn}^{DM}D_n \tag{2.3.22b}$$

where

$$u^{V}_{m} = \int_{V} \vec{f}^{V}_{m}(\vec{r}) \cdot \vec{E}^{i} d\vec{r}, \quad u^{S}_{m} = \int_{V} \vec{f}^{S}_{m}(\vec{r}) \cdot \vec{E}^{i}_{\tan} d\vec{r} \tag{2.3.23}$$

are the "voltage" or excitation components for every test/basis function and the parts Z^{MD} and Z^{DM} can be expanded as

$$Z^{MD}_{mn} = \begin{bmatrix} \dfrac{jw\mu}{4\pi} \displaystyle\int_{V_m}\int_{S_n} \vec{f}^{V}_{m}(\vec{r}) \cdot \vec{f}^{S}_{n}(\vec{r}\,')\, g\, d\vec{r}\,' d\vec{r} \\ -\dfrac{j}{4\pi w\varepsilon} \left\{ \begin{array}{l} \displaystyle\int_{V_m}\int_{S_n} \left(\nabla \cdot \vec{f}^{V}_{m}(\vec{r})\right)\left(\nabla \cdot \vec{f}^{S}_{n}(\vec{r}\,')\right) g\, d\vec{r}\,' d\vec{r} \\ \displaystyle -\int_{\Omega}\int_{S_n} \left(\vec{f}^{V}_{m}(\vec{r}) \cdot \hat{n}\right)\left(\nabla \cdot \vec{f}^{S}_{n}(\vec{r}\,')\right) g\, d\vec{r}\,' d\vec{r} \end{array} \right\} \end{bmatrix} \tag{2.3.24}$$

$$Z^{DM}_{mn} = \begin{bmatrix} \dfrac{-w^{2}\mu}{4\pi} \displaystyle\int_{S_m}\int_{V_n} \vec{f}^{S}_{m}(\vec{r}) \cdot \vec{f}^{V}_{n}(\vec{r}\,') K_n(\vec{r}\,')\, g\, d\vec{r}\,' d\vec{r} \\ +\dfrac{1}{4\pi\varepsilon} \left\{ \begin{array}{l} \displaystyle\int_{S_m}\int_{V_n} \left(\nabla \cdot \vec{f}^{S}_{m}(\vec{r})\right)\left(\nabla \cdot \vec{f}^{V}_{n}(\vec{r}\,')\right) K_n(\vec{r}\,')\, g\, d\vec{r}\,' d\vec{r} \\ \displaystyle +\int_{S_m}\int_{\Omega} \left(\nabla \cdot \vec{f}^{S}_{m}(\vec{r})\right)\left(\vec{f}^{V}_{n}(\vec{r}\,') \cdot \nabla K_n(\vec{r}\,')\right) g\, d\vec{r}\,' d\vec{r} \end{array} \right\} \end{bmatrix} \tag{2.3.25}$$

Note that the impedance matrices (Z^{MD} and Z^{DM}) are not symmetric in this case since test functions don't coincide with the basis functions. The components of the impedance matrix are the double volume and/or surface integrals of the Green's function. Also, a relation between Z^{MD} and Z^{DM} can be derived from (2.3.24) and (2.3.25) as

$$Z^{DM} = \left(jw\hat{K}\right) \cdot Z^{MD'}$$

where $Z^{MD'}$ is the transpose of Z^{MD} matrix (the inner and outer integrals interchanged) and $\hat{K}$ is a matrix of corresponding contrast ratios.

e. RWG basis functions

Below, we recall the following properties of the surface RWG basis functions [1].

$$f_n^S(\vec{r}) = \begin{cases} \frac{l_n}{2A_n^+} \vec{r}_n^{+S} & \vec{r} \text{ in } t_n^+ \\ \frac{l_n}{2A_n^-} \vec{r}_n^{-S} & \vec{r} \text{ in } t_n^- \end{cases} \tag{2.3.26}$$

and

$$\nabla_S \cdot f_n^S(\vec{r}) = \begin{cases} \frac{l_n}{A_n^+} & \vec{r} \text{ in } T_n^+ \\ -\frac{l_n}{A_n^-} & \vec{r} \text{ in } T_n^- \end{cases} \tag{2.3.27}$$

Substitution of equations (2.3.26), (2.3.27) into equation (2.3.24) gives the components of the impedance matrix in terms of RWG basis functions.

$$\int_V \int_S \vec{f}_m^{\,V}(\vec{r}) \cdot \vec{f}_n^{\,S}(\vec{r}\,')gd\vec{r}'d\vec{r} =$$
$$+\frac{a_m \ell_n}{6V_m^+ A_n^+} \int_{T_m^+} \int_{t_n^+} \left(\vec{r}_m^{\,V+}(\vec{r}) \cdot \vec{r}_n^{\,S+}(\vec{r}\,')\right)gd\vec{r}\,'d\vec{r} + \frac{a_m \ell_n}{6V_m^+ A_n^-} \int_{T_m^+} \int_{t_n^-} \left(\vec{r}_m^{\,V+}(\vec{r}) \cdot \vec{r}_n^{\,S-}(\vec{r}\,')\right)gd\vec{r}\,'d\vec{r} \qquad (2.3.28)$$
$$+\frac{a_m \ell_n}{6V_m^- A_n^+} \int_{T_m^-} \int_{t_n^+} \left(\vec{r}_m^{\,V-}(\vec{r}) \cdot \vec{r}_n^{\,S+}(\vec{r}\,')\right)gd\vec{r}\,'d\vec{r} + \frac{a_m \ell_n}{6V_m^- A_n^-} \int_{T_m^-} \int_{t_n^-} \left(\vec{r}_m^{\,V-}(\vec{r}) \cdot \vec{r}_n^{\,S-}(\vec{r}\,')\right)gd\vec{r}\,'d\vec{r}$$

$$\int_V \int_S \nabla \cdot \vec{f}_m^{\,V}(\vec{r}) \nabla \cdot \vec{f}_n^{\,S}(\vec{r}\,')gd\vec{r}'d\vec{r} =$$
$$+\frac{a_m \ell_n}{V_m^+ A_n^+} \int_{T_m^+} \int_{t_n^+} gd\vec{r}d\vec{r}\,' - \frac{a_m \ell_n}{V_m^+ A_n^-} \int_{T_m^+} \int_{t_n^-} gd\vec{r}\,'d\vec{r} - \frac{a_m \ell_n}{V_m^- A_n^+} \int_{T_m^-} \int_{t_n^+} gd\vec{r}\,'d\vec{r} + \frac{a_m \ell_n}{V_m^- A_n^-} \int_{T_m^-} \int_{t_n^-} gd\vec{r}\,'d\vec{r} \qquad (2.3.29)$$

$$\int_\Omega \int_S \left(\vec{f}_n^{\,S}(\vec{r}) \cdot \hat{n}\right)\left(\nabla \cdot \vec{f}_n^{\,S}(\vec{r}\,')\right)gd\vec{r}'d\vec{r} = \frac{\ell_n}{A_n^+} \int_{S_m} \int_{t_n^+} gd\vec{r}\,'d\vec{r} - \frac{\ell_n}{A_n^-} \int_{S_m} \int_{t_n^-} gd\vec{r}\,'d\vec{r} \qquad (2.3.30)$$

Now, we recall the following properties of the volume RWG basis functions [2].

$$f_n^{\,V}(\vec{r}) = \begin{cases} \frac{a_n}{3V_n^+} \vec{r}_n^{\,+V} & \vec{r} \ in \ T_n^+ \\ \frac{a_n}{3V_n^-} \vec{r}_n^{\,-V} & \vec{r} \ in \ T_n^- \end{cases} \qquad (2.3.31)$$

$$\nabla_V \cdot f_n^{\,V}(\vec{r}) = \begin{cases} \frac{a_n}{V_n^+} & \vec{r} \ in \ T_n^+ \\ -\frac{a_n}{V_n^-} & \vec{r} \ in \ T_n^- \end{cases} \qquad (2.3.32)$$

and

$$\left(\vec{f}_n^{\,V}(\vec{r})\cdot\hat{n}\right)=1 \quad \text{on face } n \tag{2.3.33}$$

Substitution of equations (2.3.31), (2.3.32) into equation (2.3.25) gives the components of the impedance matrix in terms of RWG basis functions.

$$\begin{aligned}
&\int_S\int_V \vec{f}_m^{\,S}(\vec{r})\cdot\vec{f}_n^{\,V}(\vec{r}\,')K_n(\vec{r}\,')g d\vec{r}\,' d\vec{r} = \\
&+\frac{\ell_m a_n}{6A_m^+V_n^+}\int_{t_m^+}\int_{T_n^+}\left(\vec{r}_m^{\,S+}(\vec{r})\cdot\vec{r}_n^{\,V+}(\vec{r}\,')\right)K_n(\vec{r}\,')g d\vec{r}\,' d\vec{r}+\frac{\ell_m a_n}{6A_m^+V_n^-}\int_{t_m^+}\int_{T_n^-}\left(\vec{r}_m^{\,S+}(\vec{r})\cdot\vec{r}_n^{\,V-}(\vec{r}\,')\right)K_n(\vec{r}\,')g d\vec{r}\,' d\vec{r} \\
&+\frac{\ell_m a_n}{6A_m^-V_n^+}\int_{t_m^-}\int_{T_n^+}\left(\vec{r}_m^{\,S-}(\vec{r})\cdot\vec{r}_n^{\,V+}(\vec{r}\,')\right)K_n(\vec{r}\,')g d\vec{r}\,' d\vec{r}+\frac{\ell_m a_n}{6A_m^-V_n^-}\int_{t_m^-}\int_{T_n^-}\left(\vec{r}_m^{\,S-}(\vec{r})\cdot\vec{r}_n^{\,V-}(\vec{r}\,')\right)K_n(\vec{r}\,')g d\vec{r}\,' d\vec{r}
\end{aligned} \tag{2.3.34}$$

$$\begin{aligned}
&\int_S\int_V \nabla\cdot\vec{f}_m^{\,S}(\vec{r})\nabla\cdot\vec{f}_n^{\,V}(\vec{r}\,')K_n(\vec{r}\,')g d\vec{r}\,' d\vec{r} = \\
&+\frac{\ell_m a_n}{A_m^+V_n^+}\int_{t_m^+}\int_{T_n^+}K_n(\vec{r}\,')g d\vec{r}\, d\vec{r}\,'-\frac{\ell_m a_n}{A_m^+V_n^-}\int_{t_m^+}\int_{T_n^-}K_n(\vec{r}\,')g d\vec{r}\,' d\vec{r} \\
&-\frac{\ell_m a_n}{A_m^-V_n^+}\int_{t_m^-}\int_{T_n^+}K_n(\vec{r}\,')g d\vec{r}\,' d\vec{r}+\frac{\ell_m a_n}{A_m^-V_n^-}\int_{t_m^-}\int_{T_n^-}K_n(\vec{r}\,')g d\vec{r}\,' d\vec{r}
\end{aligned} \tag{2.3.35}$$

$$\begin{aligned}
&\int_S\int_\Omega\left(\nabla\cdot\vec{f}_m^{\,S}(\vec{r})\right)\left(\vec{f}_n^{\,V}(\vec{r}\,')\cdot\nabla K_n(\vec{r}\,')\right)g d\vec{r}\,' d\vec{r} = \\
&\frac{\ell_m\left(K_n^+-K_n^-\right)}{A_m^+}\int_{t_m^+}\int_{S_n}g d\vec{r}\,' d\vec{r}-\frac{\ell_m\left(K_n^+-K_n^-\right)}{A_m^-}\int_{t_m^-}\int_{S_n}g d\vec{r}\,' d\vec{r}
\end{aligned} \tag{2.3.36}$$

f. Integral calculation

Following a similar procedure to section 2.1 and 2.2, we take a closer look at the integral calculations that form the major part of the impedance matrix calculations. Consider a structure where all tetrahedral volumes are enumerated by $p = 1,...,P$ and all triangular surface patches are enumerated by $q = 1,...,Q$.

Then, every integral in equation (2.3.28) is build upon the term

$$A_{VSpq}^{ij} = \int_{T_p}\int_{t_q} \left(\vec{r}_i^{\,V} \cdot \vec{r}\,'^{S}_j\right) g(|\vec{r} - \vec{r}\,'|) d\vec{r}\,' d\vec{r} \quad p = 1,...,P \quad q = 1,...,Q \quad i = 1,2,3,4 \quad j = 1,2,3 \tag{2.3.37}$$

Also, every integral in equation (2.3.29) is build upon the term

$$\Phi_{VSpq}^{1} = \int_{T_p}\int_{t_q} g(|\vec{r} - \vec{r}\,'|) d\vec{r}\,' d\vec{r} \quad p = 1,...,P \quad q = 1,...,Q \tag{2.3.38}$$

Every integral in equation (2.3.30) is build upon the term

$$\Phi_{Vpq}^{2} = \int_{S_p}\int_{t_q} g(|\vec{r} - \vec{r}\,'|) d\vec{r}\,' d\vec{r} \quad p = 1,...,P \quad q = 1,...,Q \tag{2.3.39}$$

Similarly in case of Z^{DM}, every integral in equation (2.3.34) is build upon the term

$$A_{SVpq}^{ji} = \int_{t_q}\int_{T_p} \left(\vec{r}_j^{\,S} \cdot \vec{r}\,'^{V}_i\right) g(|\vec{r} - \vec{r}\,'|) d\vec{r}\,' d\vec{r} \quad p = 1,...,P \quad q = 1,...,Q \quad i = 1,2,3,4 \quad j = 1,2,3 \tag{2.3.40}$$

Also, every integral in equation (2.3.35) is build upon the term

$$\Phi^{1}_{SVpq} = \int_{T_q}\int_{t_p} g(|\vec{r} - \vec{r}'|)d\vec{r}'d\vec{r} \quad p = 1,...,P \quad q = 1,...,Q \tag{2.3.41}$$

Every integral in equation (2.3.36) is build upon the term

$$\Phi^{2}_{\Omega Spq} = \int_{S_q}\int_{t_p} g(|\vec{r} - \vec{r}'|)d\vec{r}'d\vec{r} \quad p = 1,...,P \quad q = 1,...,Q \tag{2.3.42}$$

Here, $\vec{r}_i = \vec{r} - \vec{r}_i'$ for any vertex *i* of tetrahedron *p* whereas $\vec{r}'_j = \vec{r}' - \vec{r}_j'$ for any vertex *j* of triangle *q*. The integrals (2.3.37)-(2.3.42) are found using a vectorized routine, which employs Gaussian integration [13], [15] as discussed in sections 2.1 and 2.2. Calculation is performed over all tetrahedral/triangular elements, not over RWG basis functions. The corresponding formulas are given in Appendix B.

3. Test results of simulations

The MoM equations derived in sections 2.1, 2.2, 2.3 were implemented in the form of Matlab scripts. The solver was then tested for pure metallic (radiation), pure dielectric (scattering) and combined metal-dielectric structure (radiation and scattering). This section provides a summary of the test results obtained in each case.

3.1 Test of simulations for a pure metallic patch antenna (radiation)

In this section, simulation of a simple structure of an air-filled metal patch antenna is tested for different mesh configurations. The simulations are based on the derivation in section 2.1. Error in the calculation of resonant frequency is reported for each case.

a. Structure under study

The structure under study is comprised of a simple patch antenna consisting of a single patch above a finite ground plane. The dimensions of the patch are 2 by 4 cm on a 4 by 8 cm ground plane, with the thickness of the substrate (air-filled) 0.5 cm. A typical structure with base grid size 4 by 8 (in x, y directions respectively,) is shown in Fig.3.1.1. This structure has 117 surface RWG elements.

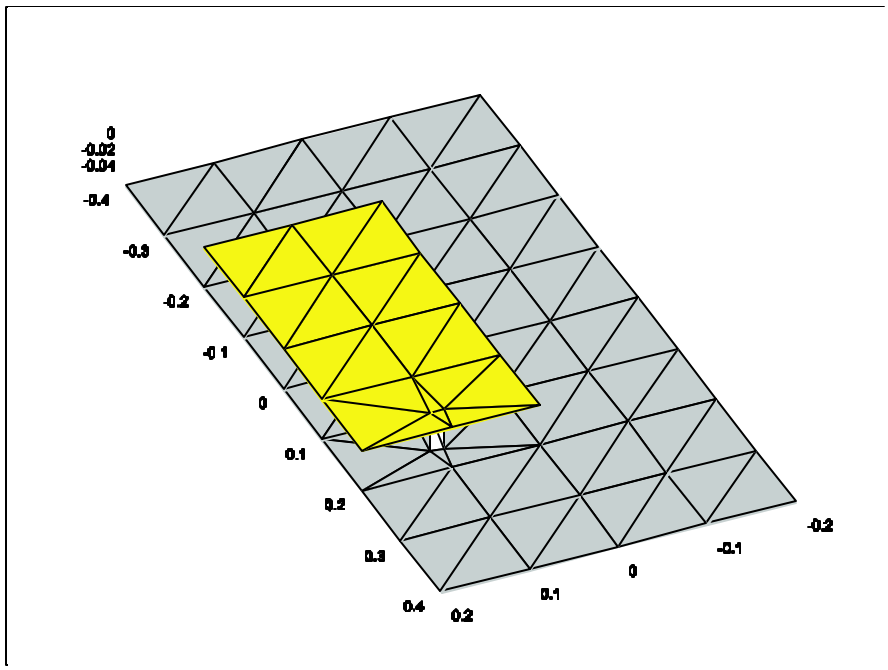

Fig.3.1.1 Metal patch antenna structure

(Grid Size: 4x8, Feed Division: 1, Patch Border rendering: 0)

b. Test results

The variation of real and imaginary part of the impedance over a suitable frequency range was considered. The results were compared with those obtained by using ANSOFT HFSS. Comparison results for the basic mesh configuration in Fig.3.1.1 can be seen in Fig.3.1.2. The error in the calculation of resonant frequency was found to be 2.04 percent. The execution time per frequency step in this case was 0.22 sec as compared to 3-4 min for ANSOFT HFSS.

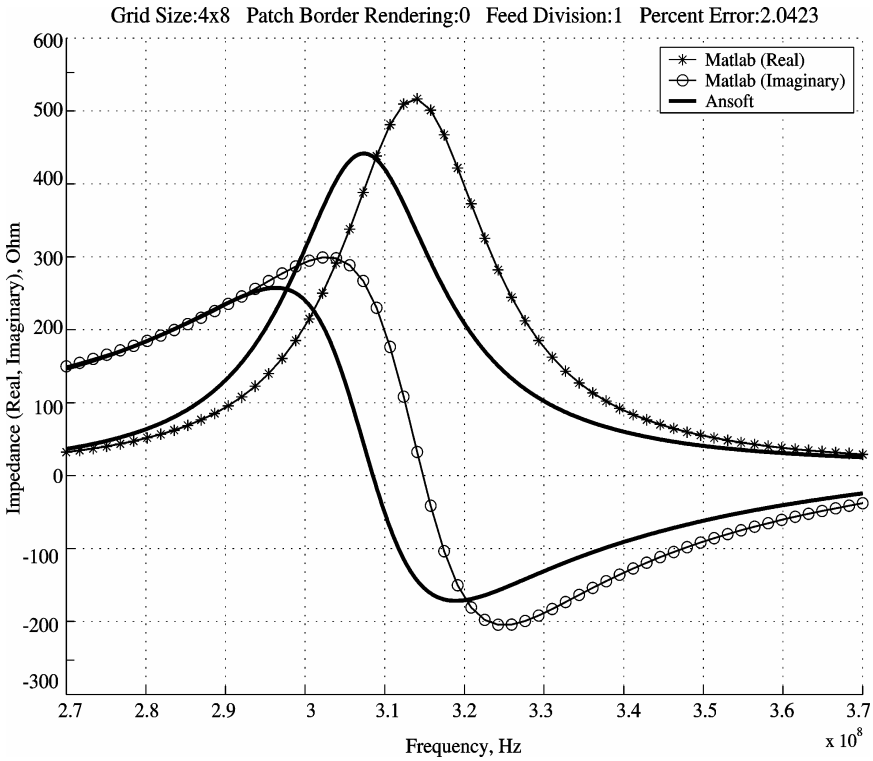

Fig.3.1.2 Test results for the basic structure

(Grid Size: 4x8, Feed Division: 1, Patch Border rendering: 0)

Tests were performed for different mesh configurations including higher level of feed discretization and patch border rendering. It can be observed that the performance of the solver was improved (error: 1.19 percent, execution time per frequency step: 0.25 sec) for the structure with higher patch border rendering as shown in Fig.3.1.3.

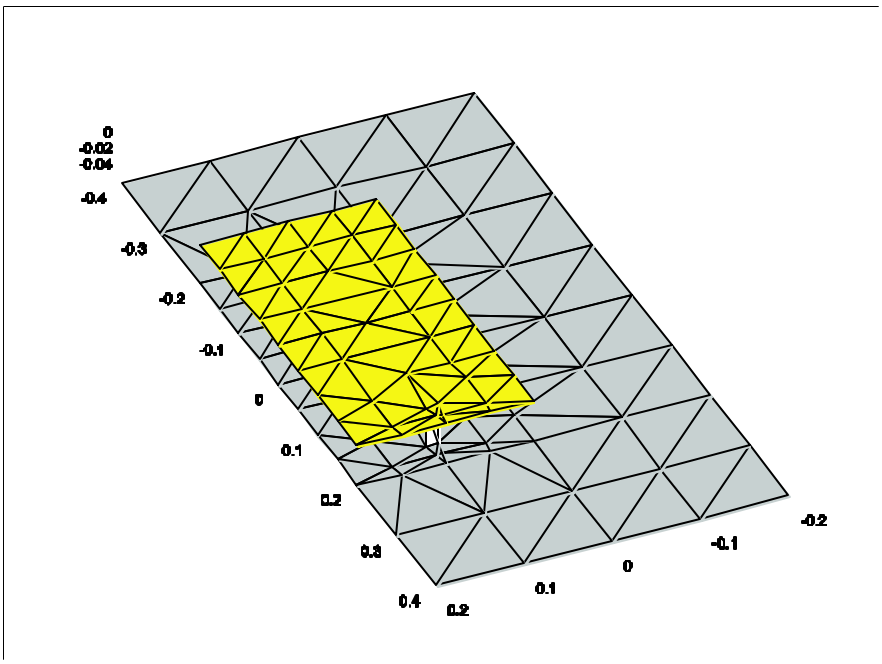

Fig.3.1.3 Metal patch antenna structure

(Grid Size: 4x8, Feed Division: 1, Patch Border rendering: 1)

Similar improvement in the solver performance was observed when the feed discretization level was increased. The result can be seen in Fig.3.1.4. (error: 0.49 percent, execution time per frequency step: 0.96 sec) .

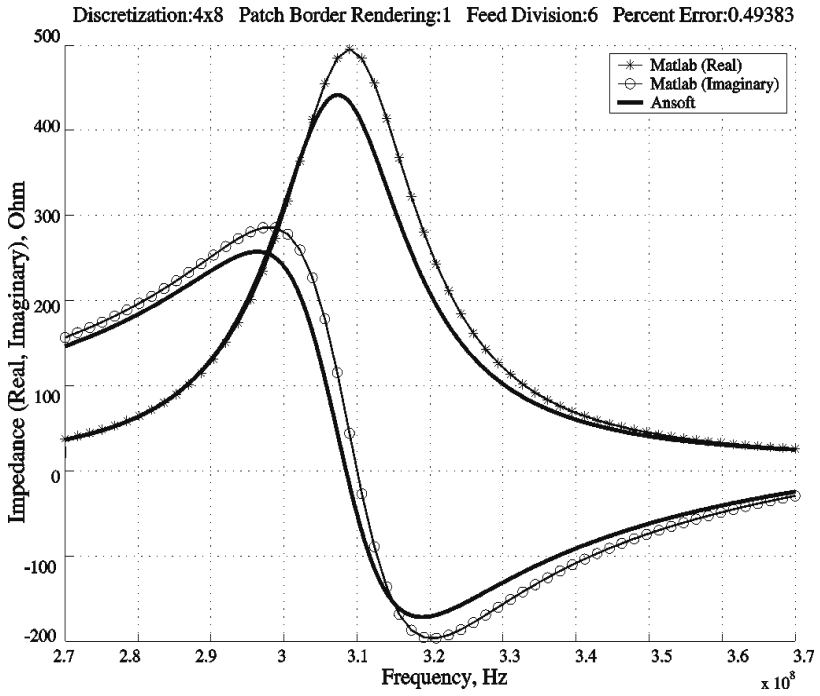

Fig.3.1.4 Test results for structure with patch border rendering

(Grid Size: 4x8, Feed Division: 1, Patch Border rendering: 1)

The performance is further improved if the base grid is refined as shown in Fig.3.1.5. Similar tests were performed on the refined (6x12) structure. In the best case (Base Grid: 6x12, Patch Border Rendering: 2, Feed Discretization: 6), the error in the calculation of the resonant frequency was found to be 0.21 percent (Fig.3.1.6). The execution time per frequency step in this case was 8.53 sec as compared to 3-4 min for ANSOFT HFSS.

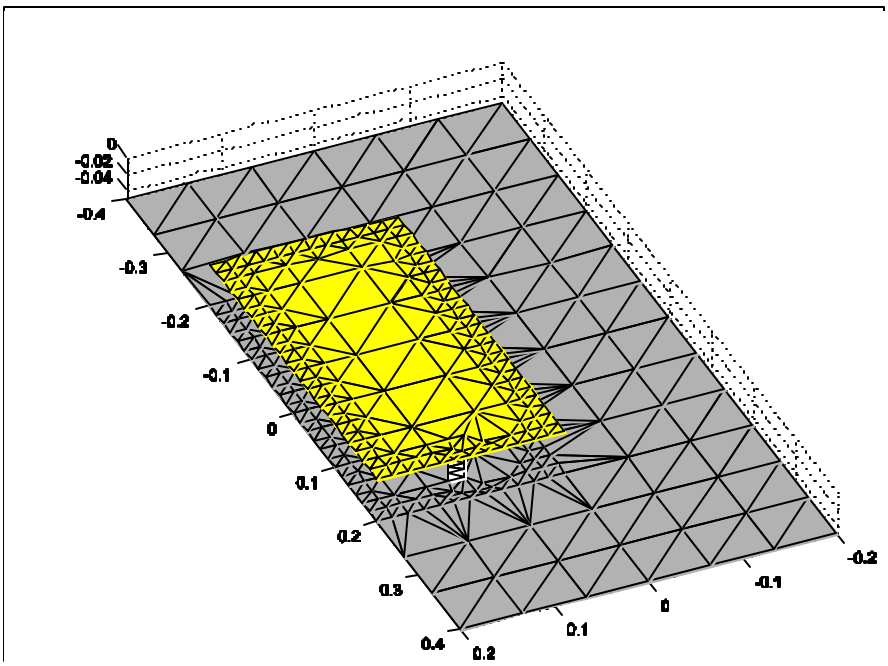

Fig.3.1.5 Metal patch antenna structure

(Grid Size: 6x12, Feed Division: 6, Patch Border rendering: 2)

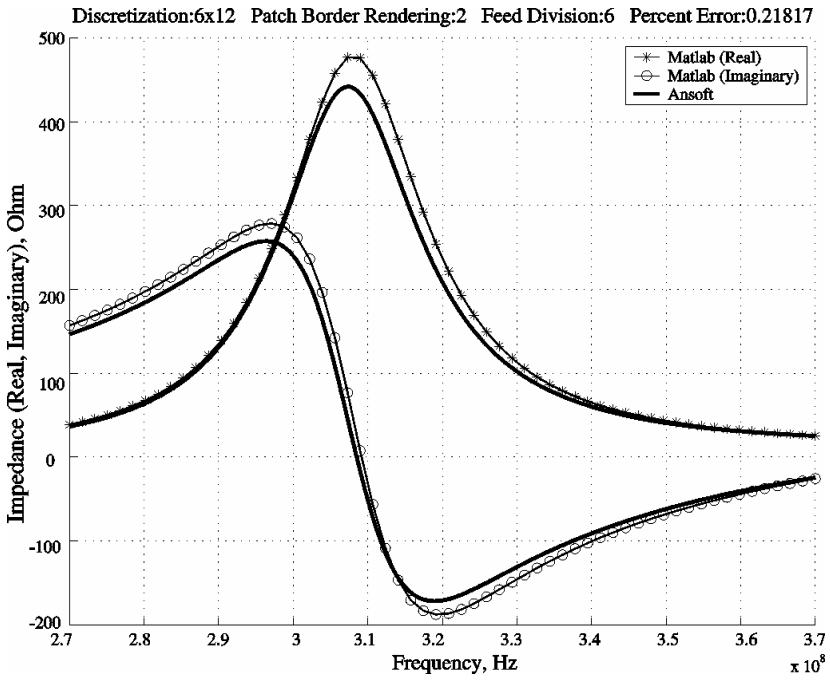

Fig.3.1.6 Test results for the best case

(Grid Size: 6x12, Feed Division: 6, Patch Border rendering: 2)

The test results are summarized in Table 3.1a, 3.1b and 3.1c. Nf denotes the level of feed discretization. A steady improvement is observed with higher mesh refinement.

Table 3.1a: Test results-1 for pure metal patch antenna

Value of Nf	4 by 8 Discritization (Patch border rendering: 0)		6 by 12 Discritization (Patch border rendering: 0)	
	Number of RWG edge elements	Percent Error	Number of RWG edge elements	Percent Error
1	117	2.04	258	1.93
2	119	1.68	260	1.60
3	121	1.56	262	1.49
6	127	1.40	268	1.31

Table 3.1b: Test results-2 for pure metal patch antenna

Value of Nf	4 by 8 Discritization (Patch border rendering: 1)		6 by 12 Discritization (Patch border rendering: 1)	
	Number of RWG edge elements	Percent Error	Number of RWG edge elements	Percent Error
1	265	1.19	486	1.19
2	267	0.84	488	0.83
3	269	0.68	490	0.68
6	275	0.49	496	0.47

Table 3.1c: Test results-3 for pure metal patch antenna

Value of Nf	4 by 8 Discritization (Patch border rendering: 2)		6 by 12 Discritization (Patch border rendering: 2)	
	Number of RWG edge elements	Percent Error	Number of RWG edge elements	Percent Error
1	597	0.92	990	0.93
2	599	0.57	992	0.58
3	601	0.43	994	0.43
6	607	0.22	1000	0.21

3.2 Test of simulations for a pure dielectric structure (scattering)

In this section, simulation of a pure dielectric structure is tested for different dielectric constants and different mesh configurations. The simulations are based on the derivation given in section 2.2. Error in the calculation of magnitude of scattered electric field is reported for various cases.

a. Structure under study

The structure under study is comprised of a dielectric volume of dimensions 4 by 8 by 0.5 cm. A typical structure with base grid size 4 by 8 (in x, y directions respectively,) is shown in Fig.3.2.1. This structure has 472 volume RWG elements.

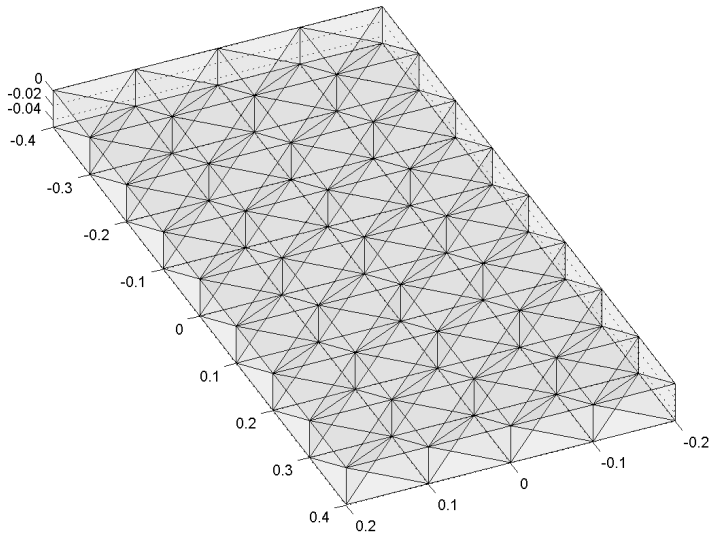

Fig.3.2.1 Pure dielectric structure

(Grid Size: 4x8, Number of layers: 1)

b. Test results

Normal incidence of a linearly polarized wave along the Z-axis was considered. The variation of magnitude of the scattered field along the X or Y-axis was computed. The results were compared with those obtained by using ANSOFT HFSS. Tests were carried out at two frequencies for each e_r of the substrate. One frequency was in the lower range as compared to the resonant frequency and the second one was considered near the resonance region. E.g. for e_r 10 of the substrate, tests were carried out for 75 and 125 MHz. Agreement with ANSOFT was found to be better at lower frequencies as compared to those near resonant frequencies. Results for higher frequencies are presented in this section. Comparison results for the basic mesh configuration in Fig.3.2.1 can be seen in Fig.3.2.2. Only the dominant component of the scattered field is plotted in Fig.3.2.2. The steps in the

plot are inherent to the computation method since, the magnitude of electric field is constant inside a single tetrahedron.

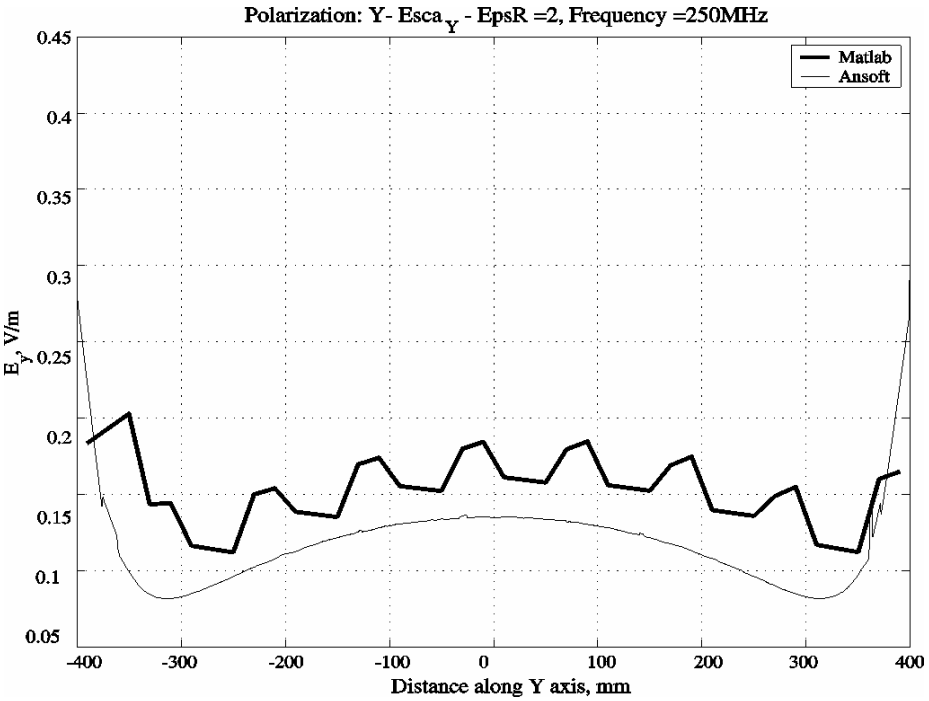

Fig.3.2.2 Test results for the basic structure

(e_r: 2, Grid Size: 4x8, Number of layers: 1)

Computations for different dielectric constants for the same structure (Fig.3.2.1) were done and it was observed that for a given mesh, the agreement with ANSOFT improves as the dielectric constant increases. Test results for dielectric constant 10 can be seen in Fig.3.2.3.

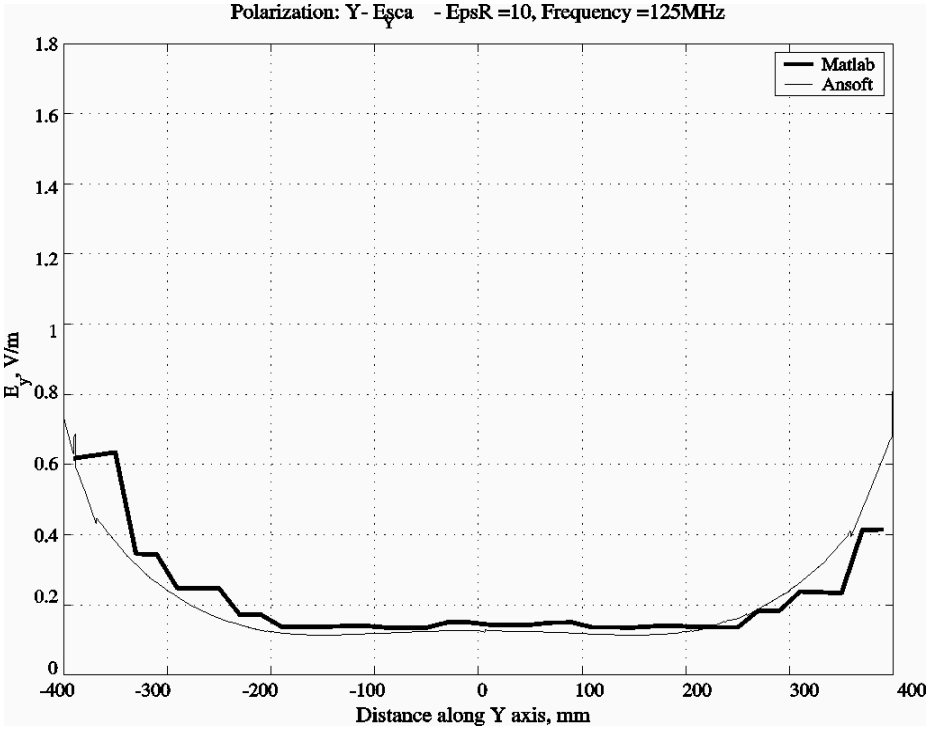

Fig.3.2.3 Test results for the basic structure

(e_r: 10, Grid Size: 4x8, Number of layers: 1)

For higher order of base grid size (6x12) improvement in the agreement (even for lower dielectric constants) is observed. Fig.3.2.4 shows results for e_r = 2.

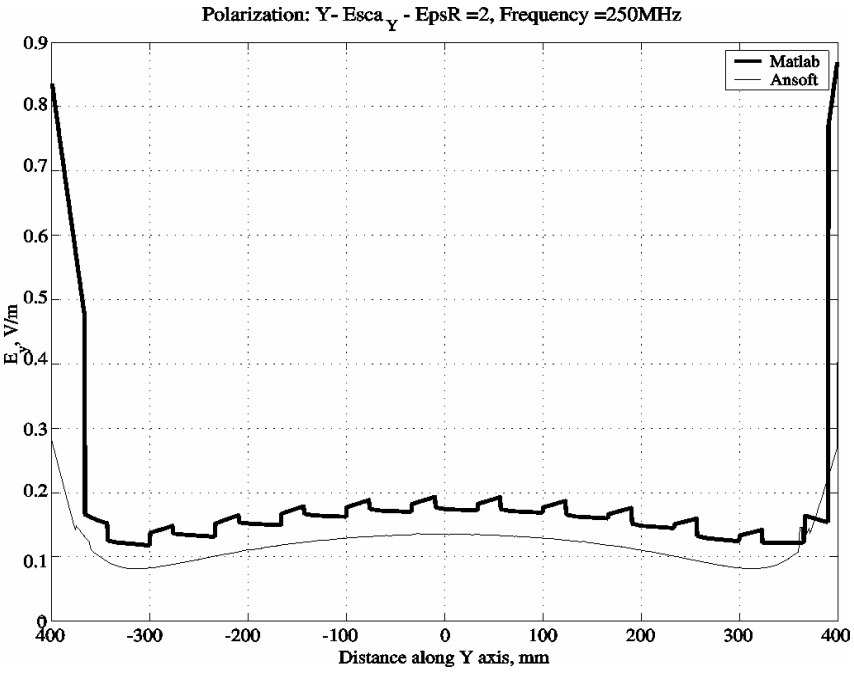

Fig.3.2.4 Test results for the refined structure

(e_r: 2, Grid Size: 6x12, Number of layers: 1)

Also, computations for two layers of volume elements were done for e_r: 2. The structure is shown in Fig.3.2.5. The number of volume RWG elements for this structure is 1944. The results for this structure can be seen in Fig.3.2.6. As can be observed the agreement is considerably improved as compared to those for the rough structure (Fig.3.2.2)

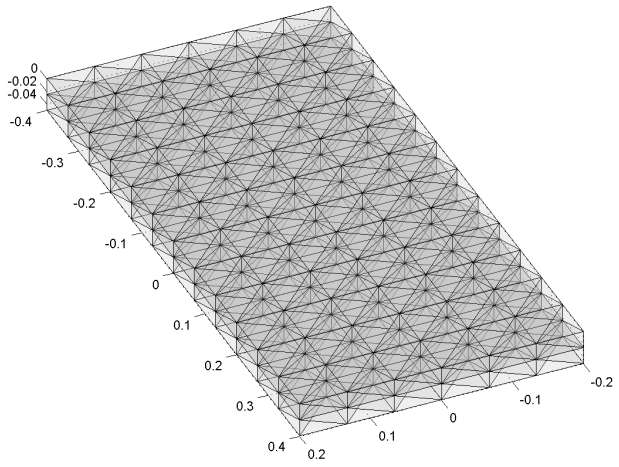

Fig.3.2.5 Refined dielectric structure

(e_r: 2, Grid Size: 6x12, Number of layers: 2)

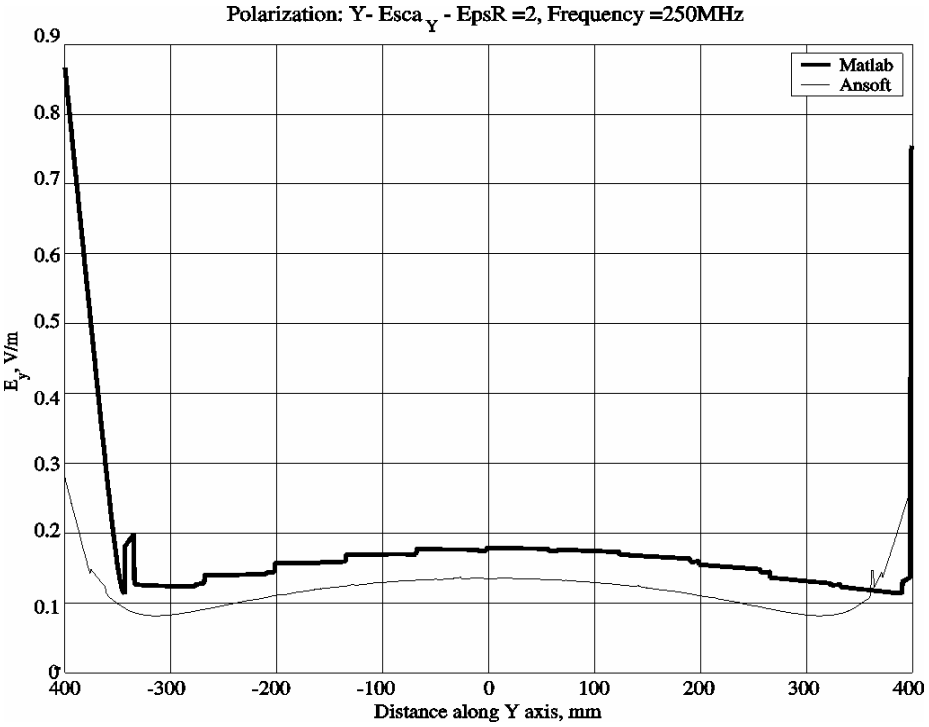

Fig.3.2.6 Test results for the refined structure

(e_r: 2, Grid Size: 6x12, Number of layers: 2)

3.3 Test of simulations for a combined metal-dielectric structure

In this section, simulation of a combined metal-dielectric object (a scatterer) is tested for different dielectric constants and different mesh configurations. The simulations are based on the derivations given in sections 2.1, 2.2 and 2.3. Error in the calculation of magnitude of scattered electric field is reported for various cases.

a. Structure under study

The structure under study is comprised of the dielectric structure of dimensions 4 by 8 by 0.5 cm (from section 3.2) with an attached metal ground plane. A typical structure with base grid size 4 by 8 (in x, y directions respectively,) is shown in Fig.3.3.1. This structure has 84 surface RWG elements and 472 volume RWG elements.

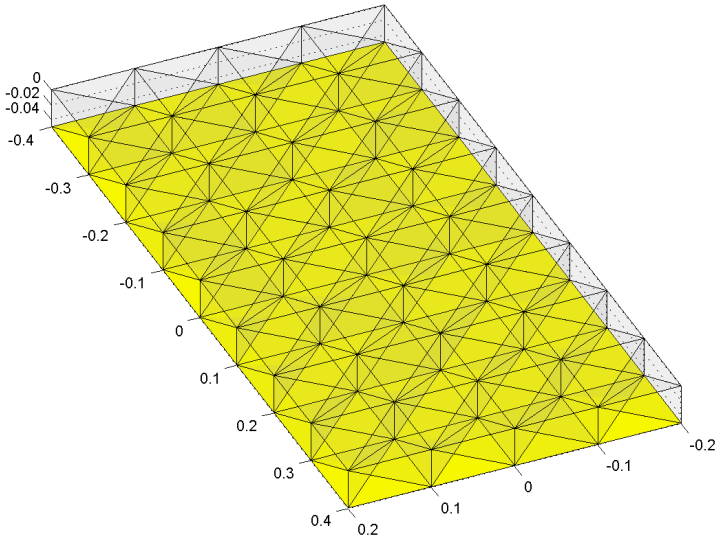

Fig.3.3.1 Metal - dielectric structure (Grid Size: 4x8)

b. Test results

Normal incidence of a linearly polarized wave along Z-axis was considered. The variation of magnitude of the scattered field along X or Y-axis was computed. Similar to section 3.2, tests were carried out at two frequencies for each e_r of the substrate. The results were compared with those obtained by using ANSOFT HFSS. A trend similar to section 3.2 was observed in the results for various cases i.e.

(i) It was observed that for a given mesh, the agreement with ANSOFT improves as the dielectric constant increases.

(ii) Agreement with ANSOFT was found to be better at lower frequencies as compared to those near resonant frequencies.

Test results for incidence of a 75 MHz wave for the structure in Fig.3.3.1 with dielectric constant 10 can be seen in Fig.3.3.2. Only the dominant component of the scattered field is plotted in Fig.3.3.2.

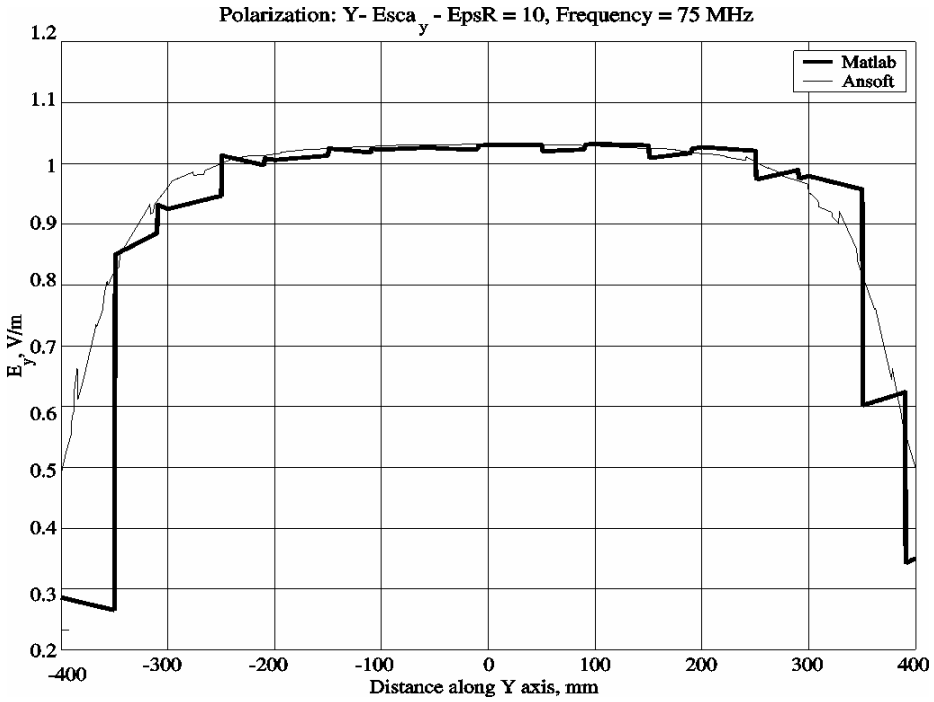

Fig.3.3.2 Test results for the metal-dielectric structure at 75 MHz

(e_r: 10, Grid Size: 4x8)

Fig.3.3.3 shows comparison with ANSOFT for the same structure at 125 MHz. The agreement with ANSOFT gets worse as we compute the results for scattering near the resonant frequency. Similar observations were made for different e_r values (2, 3 and 5).

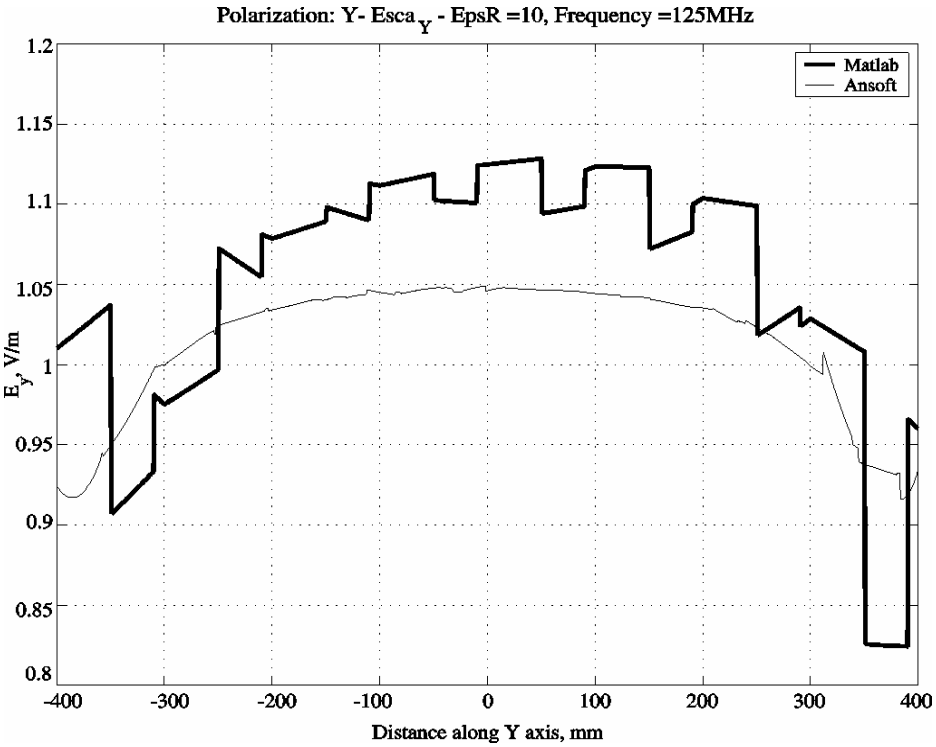

Fig.3.3.4 Test results for the metal-dielectric structure at 125 MHz

(e_r: 10, Grid Size: 4x8)

Improved results are obtained for structure with two layers of volume RWG elements.

3.4 Test of simulations for a patch antenna on a dielectric substrate

In this section, simulation of a simple structure of a metal patch antenna on a dielectric substrate is tested for different mesh configurations and different dielectric constants for the substrate. The simulations are based on the derivation given in section 2.1, 2.2 and 2.3. Error in the calculation of resonant frequency is reported for each case.

a. Structure under study

The structure under study is comprised of a simple patch antenna consisting of a single patch on a dielectric substrate with a finite ground plane. The dimensions of the patch are 2 by 4 cm on a 4 by 8 cm ground plane, with the thickness of the substrate 0.5 cm. A typical structure with base grid size 4 by 8 (in x, y directions respectively,) is shown in Fig.3.4.1. This structure has 117 surface RWG elements and 502 volume RWG elements (execution time per frequency step: 2.75 sec).

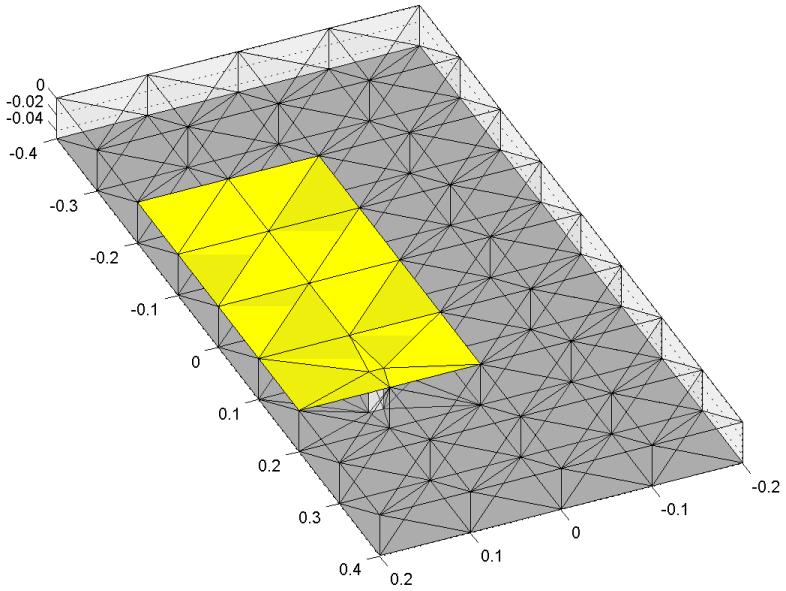

Fig.3.4.1 Patch antenna structure (on dielectric substrate)

(Grid Size: 4x8, Feed Division: 1, Patch Border rendering: 0)

b. Test results

The variation of real and imaginary part of the impedance over a suitable frequency range was plotted. The results were compared with those obtained by using ANSOFT HFSS.

Comparison results for the basic mesh configuration in Fig.3.4.1 can be seen in Fig.3.4.2. Dielectric constant of the substrate was taken as 2 in this case.

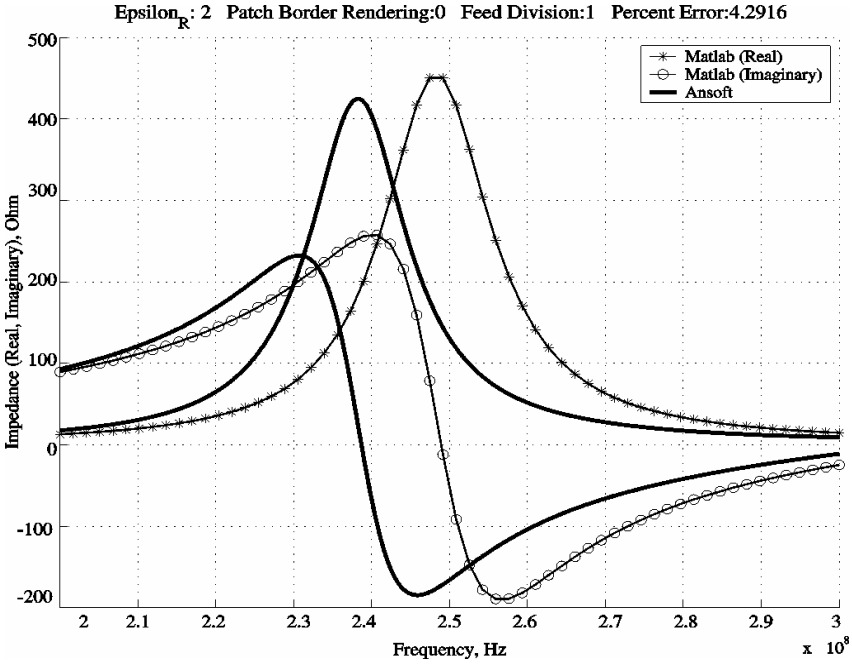

Fig.3.4.2 Test results for e_r: 2

(Grid Size: 4x8, Feed Division: 1, Patch Border rendering: 0)

For higher values of dielectric constants of the substrate higher error in the calculation of resonant frequency is observed. Fig.3.4.3 shows the result for e_r:10 for the same structure. The error is observed to be 8.09 percent as compared to 4.29 in case of e_r: 2. Table 3.3a provides the complete set of observations for this structure.

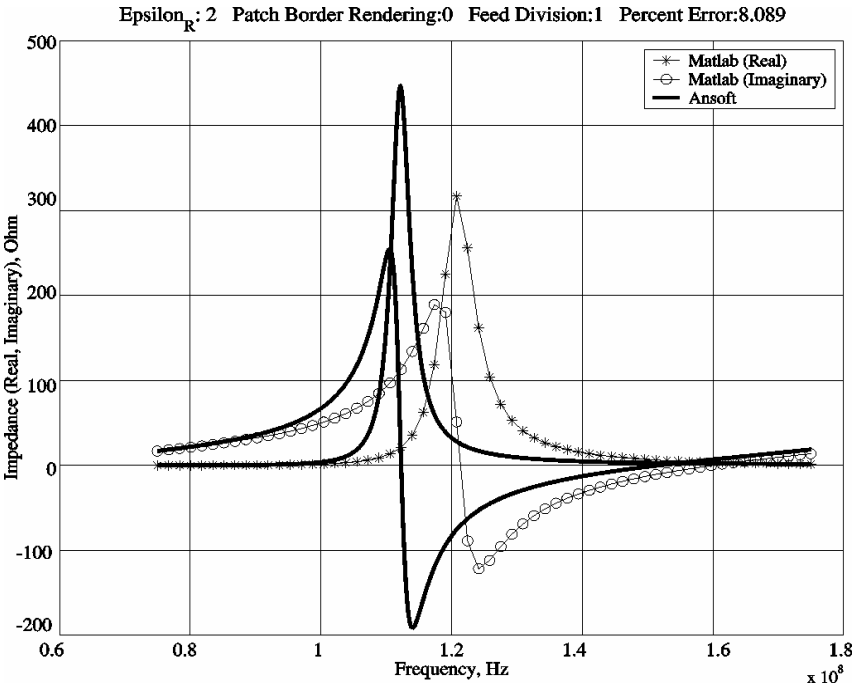

Fig.3.4.3 Test results for e_r: 10

(Grid Size: 4x8, Feed Division: 1, Patch Border rendering: 0)

Tests were performed for higher patch border rendering for different values of the dielectric constants of the substrate. Fig.3.4.4 shows the refined structure. A steady improvement on the performance was observed as compared to the previous case. Fig.3.4.5 shows the result for e_r:2 for the higher patch border rendering. The error is observed to be 3.59 percent as compared to 4.29 in case of e_r: 2. Table 3.3b provides the complete set of observations for this structure.

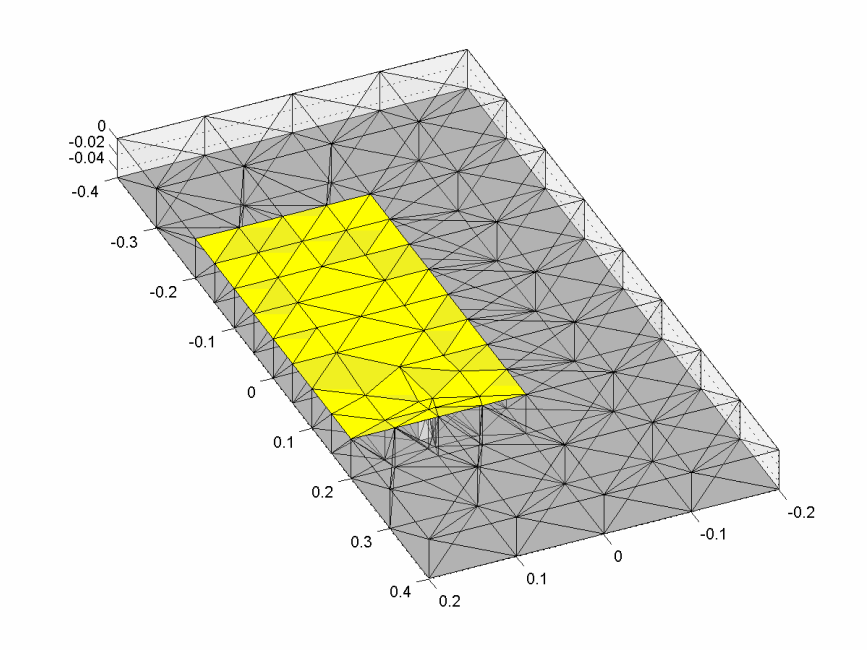

Fig.3.4.4 Refined patch antenna structure

(Grid Size: 4x8, Feed Division: 1, Patch Border rendering: 1)

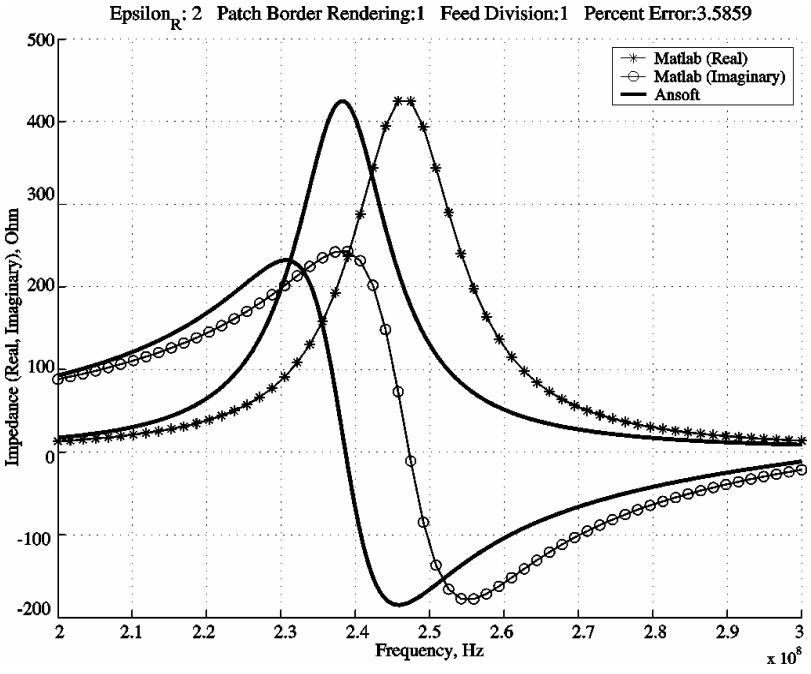

Fig.3.4.5 Test results for e_r: 2

(Grid Size: 4x8, Feed Division: 1, Patch Border rendering: 1)

Two layers of volume RWG elements were considered as shown in Fig.3.4.6. This structure has 119 surface RWG elements and 1024 volume RWG elements. Test results can be seen in Fig.3.4.7. Better agreement with ANSFOT was found for this refined structure. Table 3.3c provides results for all e_r values of the substrate.

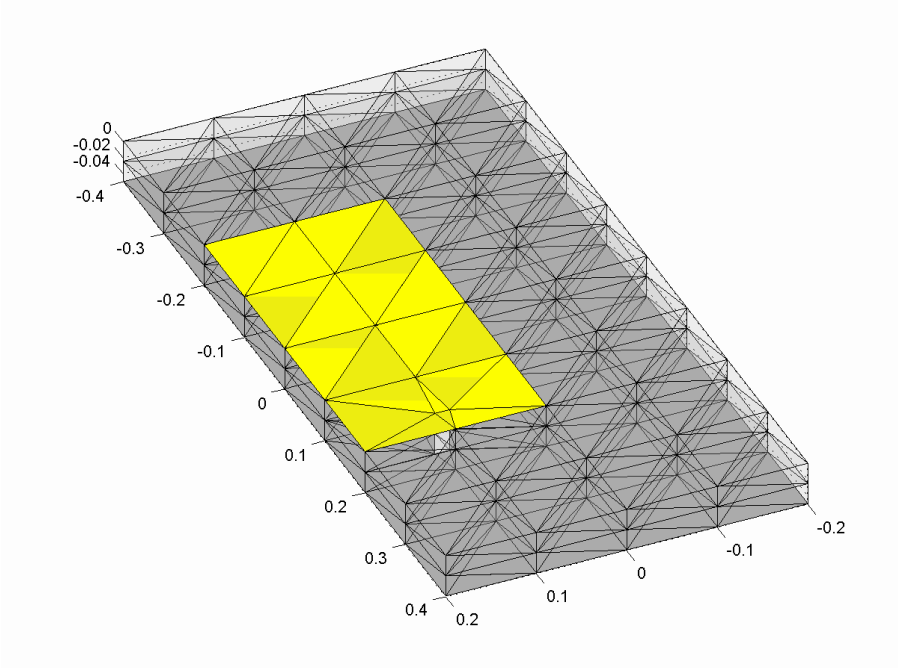

Fig.3.4.6 Patch antenna structure (2 layers)

(Grid Size: 4x8, Feed Division: 2, Patch Border rendering: 0)

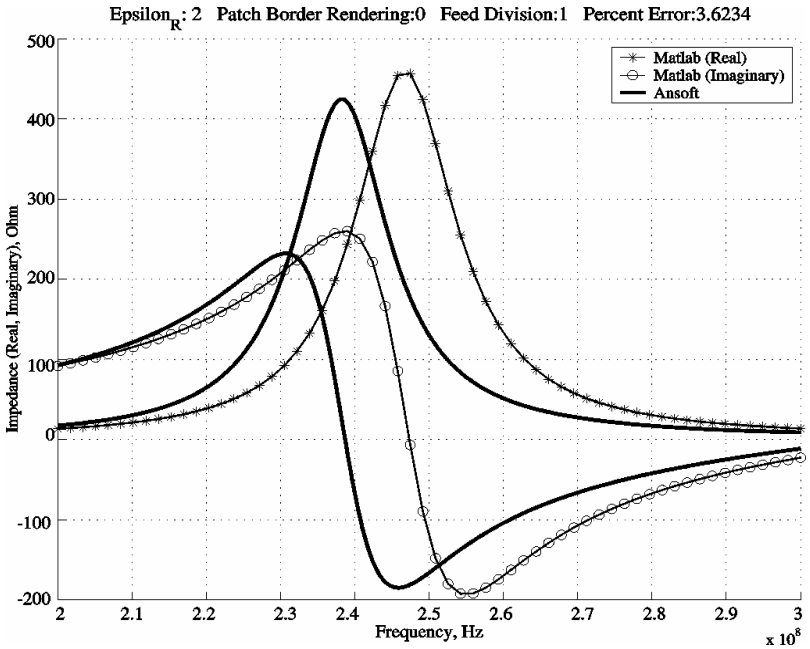

Fig.3.4.7 Test results for 2 layered patch antenna structure

(Grid Size: 4x8, Feed Division: 2, Patch Border rendering: 0)

Following similar testing procedure as for pure metal patch antenna the base grid size was increased from 4x8 to 6x12. Corresponding test results can be seen in Fig.3.4.8.

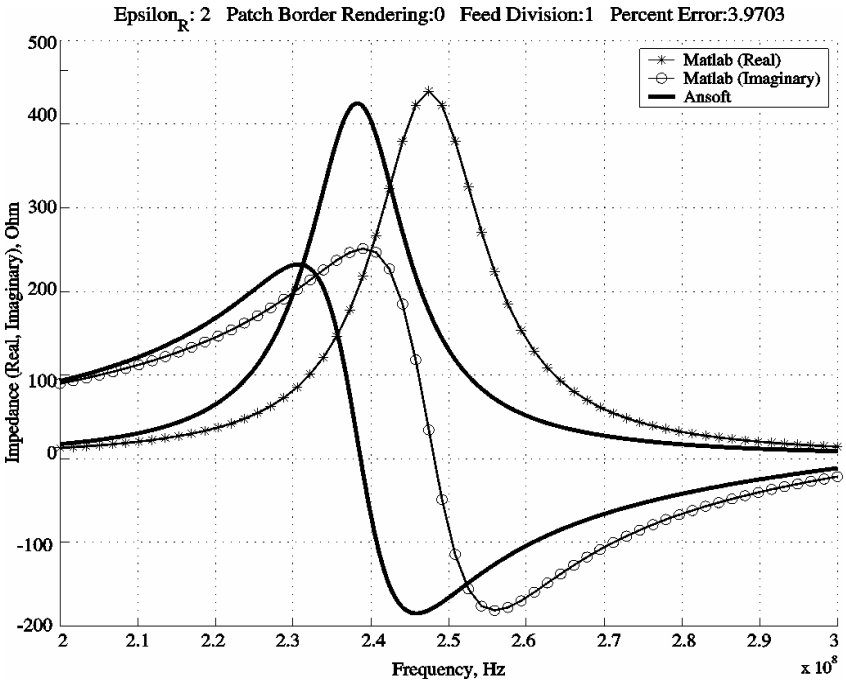

Fig.3.4.8 Test results for higher base grid size

(Grid Size: 6x12, Feed Division: 1, Patch Border rendering: 0)

Table 3.3a provides the test results for other values of e_r for this structure. An improvement in the results is seen as compared to the structure with base grid size 4x8 (Fig.3.4.1). The mesh is further refined by rendering the patch border at a higher level as shown in Fig.3.4.9 (486 surface RWG elements, 1692 volume RWG elements, execution time per frequency step: 42 sec). The improvement in the agreement can be seen in Fig.3.4.10.

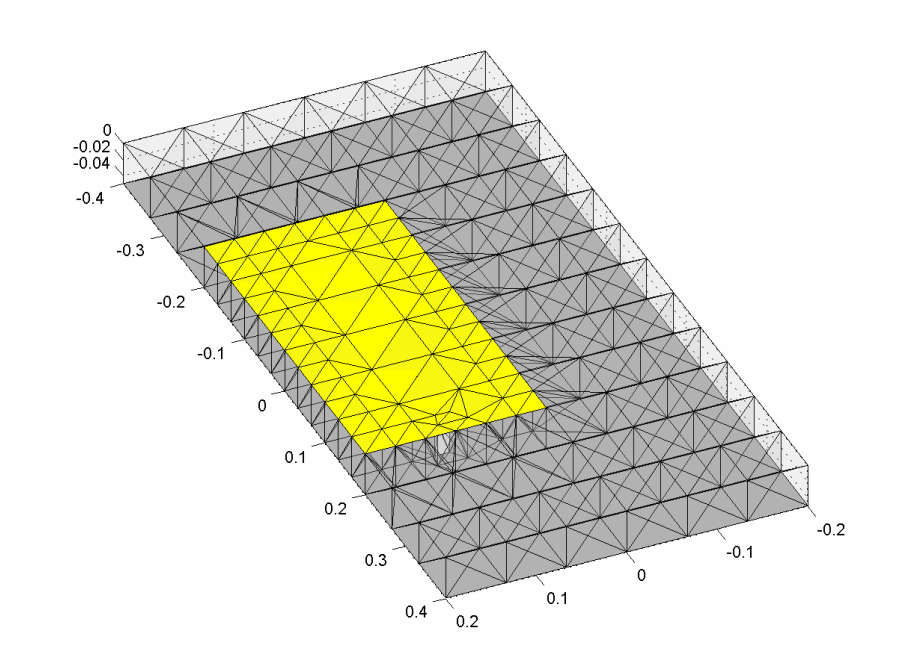

Fig.3.4.9 Structure with higher patch border rendering

(Grid Size: 6x12, Feed Division: 1, Patch Border rendering: 1)

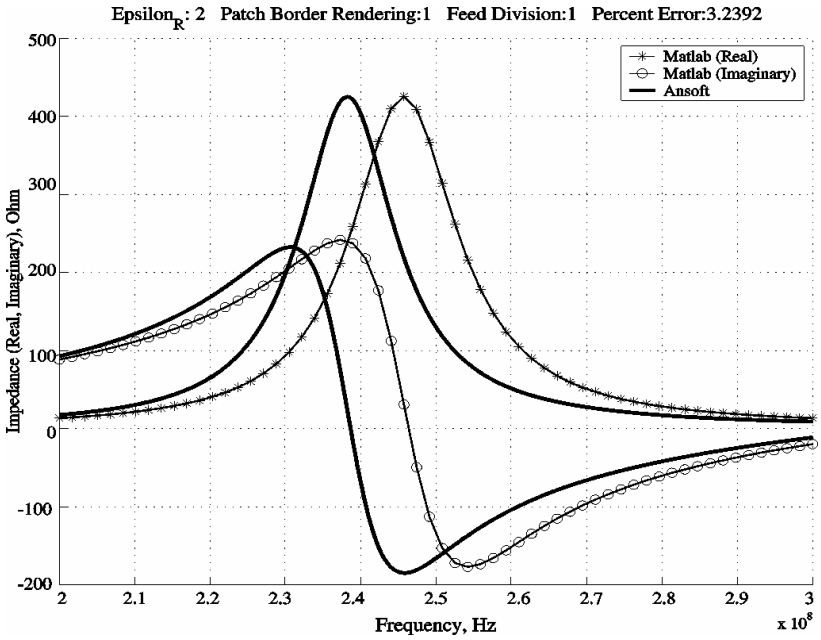

Fig.3.4.10 Test results for structure in Fig.3.4.9

(Grid Size: 6x12, Feed Division: 1, Patch Border rendering: 1)

Table 3.3a: Test results-1 for patch antenna on dielectric substrate

e_r	**Percent Error** Grid Size: 4x8 Feed division: 1, Patch border rendering: 0 Surface RWG elements: 117 Volume RWG elements: 590	**Percent Error** Grid Size: 6x12 Feed division: 1, Patch border rendering: 0 Surface RWG elements: 258 Volume RWG elements: 1262
2	4.29	3.97
3	5.61	5.17
5	7.66	7.07
10	8.09	7.33

Table 3.3b: Test results-2 for patch antenna on dielectric substrate

e_r	**Percent Error** Grid Size: 4x8 Feed division: 1, Patch border rendering: 1 Surface RWG elements: 265 Volume RWG elements: 1092	**Percent Error** Grid Size: 6x12 Feed division: 1, Patch border rendering: 1 Surface RWG elements: 486 Volume RWG elements: 1692
2	3.59	3.24
3	4.95	4.47
5	6.95	6.31
10	7.27	6.60

Table 3.3c: Test results-3 for patch antenna on dielectric substrate

e_r	**Percent Error** Grid Size: 4x8 Feed division: 2, Number of layers: 2 Patch border rendering: 0 Surface RWG elements: 119 Volume RWG elements: 1024	**Percent Error** Grid Size: 6x12 Feed division: 2, Number of layers: 2 Patch border rendering: 0 Surface RWG elements: 260 Volume RWG elements: 2000
2	3.62	3.11
3	4.79	4.16
5	6.67	5.85
10	6.91	6.09

4. Analysis of test results

Test results obtained in section 3 are analyzed in this section and methods to improve those results are proposed.

From the test results in Table 3.1a for the pure metallic (air filled) patch antenna structure, it can be seen that, for the moderate size of the grid (117 surface RWG basis functions), the error in the calculation of the resonant frequency is about 2 percent (about 7 MHz). It was also observed that the performance of the solver was more sensitive to the patch border rendering as compared to overall mesh refinement (Table 3.1b and 3.1c). Thus we can observe that there is a steady improvement in the performance as we refine the mesh. The error was considerably reduced (to about 0.22 percent) for a refined mesh with about 550 surface RWG elements.

The test results in section 3.2 with the pure dielectric structure show a similar improvement with regard to the mesh refinement for different dielectric constants in the range 1-10. At higher degree of discretization for the volume mesh (1944 volume RWG elements), near perfect agreement with ANSOFT HFSS was observed for the inner electric field within dielectric.

Keeping in mind these observations for the pure metallic and pure dielectric structure, we now take a look at the results for the patch antenna structure in section 3.4. From Table 3.3a, it can be seen that there is an improvement using higher mesh discretization but the error in the calculation of resonant frequency increases when the dielectric constant of the

substrate increases. Also, the discretization-dependent improvement was not as prominent as in case of the pure metallic structure. In this section we try to give reasoning for this matter.

As observed from the results for pure metallic structure, for the very basic structure (base grid size is 4x8), the error in the calculation of the resonant frequency was found to be 2.04 percent (Fig.3.1.2). An error of 2.04 percent for the particular frequency range (270-370 MHz), corresponds to a frequency shift of about 7 MHz. Similarly, for pure dielectric structure with the basic mesh (base grid: 4x8), the agreement with ANSOFT HFSS was not as impressive. In the case of a patch antenna structure, since it is a combined metal-dielectric structure, the errors for metal and dielectric both affect the test results. Also, as the dielectric constant of the substrate increases, the corresponding frequency range is lowered e.g. 75-175 MHz for e_r=10.

If the frequency shift of 7 MHz in the case of pure metallic structure (e_r=1) also exists in this case, it would correspond to a very high error percentage (about 7-8 percent). This is nearly the value that is observed in practice.

Hence, if the perfect agreements are to be achieved, the refined mesh (with around 550 surface RWG elements) should be chosen for the metallic part. Because the meshing of metallic structure and the underlying dielectric substrate are inter related, higher discretization for metal mesh implies higher discretization for the dielectric substrate as well. This will lead to over 2500 RWG elements and a dense impedance matrix on the size

2500x2500. The execution time for a frequency step will increase accordingly (as N^2), but accurate results can be obtained. The performance in terms of execution time and memory handling can be considerably improved by converting the Matlab scripts into C/C++ executable files and linking them with the other Matlab scripts. An improvement of several orders was observed after implementing the calculation of self/non-self MoM integrals in C.

Another reason for the error in the calculation of the resonant frequency can depend on how well the boundary conditions are satisfied at the dielectric-metal-dielectric (near the antenna feed) interface and dielectric-metal-air (boundary of dielectric surface) interface. This was briefly discussed in section 1.3. Further investigation in this direction is reported in Appendix A.

5. Conclusions

Modeling of patch antennas on arbitrary dielectric substrates using surface/volume RWG elements and the Method of Moments was implemented. Performance of the solver was tested for different mesh configurations and for different dielectric constants of the substrate. Further scope for improvement lies in the investigation of boundary conditions at the metal-dielectric interface and the optimization of the Matlab scripts.

6. References

1. S. M. Rao, D. R. Wilton, and A. W. Glisson, "Electromagnetic scattering by surfaces of arbitrary shape," *IEEE Trans. Antennas and Propagation*, vol. AP-30, no. 3, pp. 409-418, May 1982.

2. D. H. Schaubert, D. R. Wilton, and A. W. Glisson, "A tetrahedral modeling method for electromagnetic scattering by arbitrarily shaped inhomogeneous dielectric bodies," *IEEE Trans. Antennas and Propagation*, vol. AP-32, no. 1, pp. 77-85, January 1984.

3. See weblink http://www.ansoft.com/maxwellsv/ . There is really not much in the literature about the ANSOFT codes.

4. A. F. Peterson, S. L. Ray, and R. Mittra, *Computational Methods for Electromagnetics*, IEEE Press, Piscataway, New Jersey, 1998.

5. B. Kolundzija, J. Ognjanovic, and T. Sarkar, "WIPL-D Electromagnetic modeling of composite metallic and dielectric structures" Artech House, London, 2000.

6. T. Sarkar, S. M. Rao, A. R. Djordjevic, "Electromagnetic scattering and radiation from finite microstrip structures" *IEEE Trans. on Microwave Theory and Techniques*, vol. 38, pp. 1568-1575, November 1990.

7. S. M. Rao and T. K. Sarkar, "Numerical solution of time domain integral equations for arbitrarily shaped conductor/dielectric composite bodies," *IEEE Trans. Antennas and Propagation*, vol. AP-50, no. 12, pp. 1831-1837, December 2002.

8. S. Makarov, "MoM antenna simulations, with Matlab: RWG basis functions," *IEEE Trans. Antennas and Propagation*, vol. AP-43, no. 5, pp. 100-107, October 2001.

9. Yu Tiejun, Zhu Bing and Cai Wei, "Mix-RWG current basis function and its simple implementation in MoM," Microwave Symposium Digest IEEE MTT-S International, vol. 2, pp 1105-1108, 2000.

10. M. R. Abdul-Gaffoor, H. K. Smith, A. A. Kishk, and A. W. Glisson, "Simple and efficient full wave modeling of electromagnetic coupling in realistic RF multiplayer PCB layouts," *IEEE Trans. Microwave Theory and Techniques*, vol. MTT-50, no. 6, pp. 1445-1457, June 2002.

11. P. Lorrain and D. R. Corson, *Electromagnetism-Principles and Applications*, W.H. Freeman & Co., New York, 1997.

12. G. R. Cowper, "Gaussian quadrature formulas for triangles," *In.J. Numer. Meth. Eng.*, pp. 405-408, 1973.

13. O.C. Zienkiewicz and R. L. Taylor, *The Finite Element Method*, v. 1 The Basics, Butterworth-Heinemann, Oxford, 2000, 5th edition, p. 222.

14. T. F. Eibert and V. Hansen, "On the calculation of potential integrals for linear source distributions on triangular domains," *IEEE Trans. Antennas and Propagation*, vol. AP-43, no. 12, pp. 1499-1502, Dec. 1995.

15. P. Keast, "Moderate-degree tetrahedral quadrature formulas," *Computer Meth. Appl. Mechanics Eng.*, pp. 339-348, 1986.

Publications related to the thesis work

1. A. Apte and S. Makarov, "MATLAB performance for the solution of MoM equations," *18th Annual ACES Conference Proceedings*, Monterey, CA, 2002, March 2002, pp. 419-423.

2. A. Apte and S. Makarov, "Execution times for the solution of MoM equations in MATLAB," *18th 2002 IEEE-AP International Symposium*, San Antonio, TX, June 2002, pp. 692-695.

3. S. Makarov, A. Apte, and A. Berezin, "Geometry optimization of a finite array of microstrip patches using MATLAB," *18th 2002 IEEE-AP International Symposium*, San Antonio, TX, June 2002, pp. 710-713.

Appendix A

According to the equivalence theory, any Method of Moment solver should inherently satisfy the boundary conditions, thus giving accurate results for possibly moderate number of elements as compared to the Finite Element Method (FEM). Also, the performance of the MoM solver should not be dependent on the dielectric constant of the patch antenna substrate. The test results reported in section 3, were not particularly impressive since it would take at least a few thousand elements for converging to the accurate solution. Hence we decided to investigate this subject further and present the results as an Appendix to the primary part of implementing the MoM solver. We could not succeed to investigate this matter completely and this subject is open for discussion.

A test was conducted to check how well the boundary conditions on the metal-dielectric face are satisfied. As discussed in section 1.3, the condition to be satisfied at the metal-dielectric interface is:

$$r_S(\vec{r}) = \left(\frac{1}{e_R} - 1\right) s_S \qquad \text{(A.1)}$$

Hence it follows that, for all boundary faces,

$$D_n^+(K^+ - K^-) - s_S(\vec{r}) = 0 \qquad \text{(A.2)}$$

where $s_S(\vec{r})$ is the total charge density of the metal sheet (the sum of charge densities on both sides). To check the accuracy of the boundary conditions, the two quantities $D_n^+(K^+ - K^-)$ and $D_n^+(K^+ - K^-) - s_S(\vec{r})$ were plotted in Fig.A.1 for all dielectric-metal boundary faces (4x8 base grid size; eps=10) in solid and dashed lines, respectively. Thus, the dashed curve should tend to zero according to theory. But it can be seen from the plot that it is not exactly zero as it should be. Though the difference magnitudes are not high, they may be responsible for the error in the computation of resonant frequency.

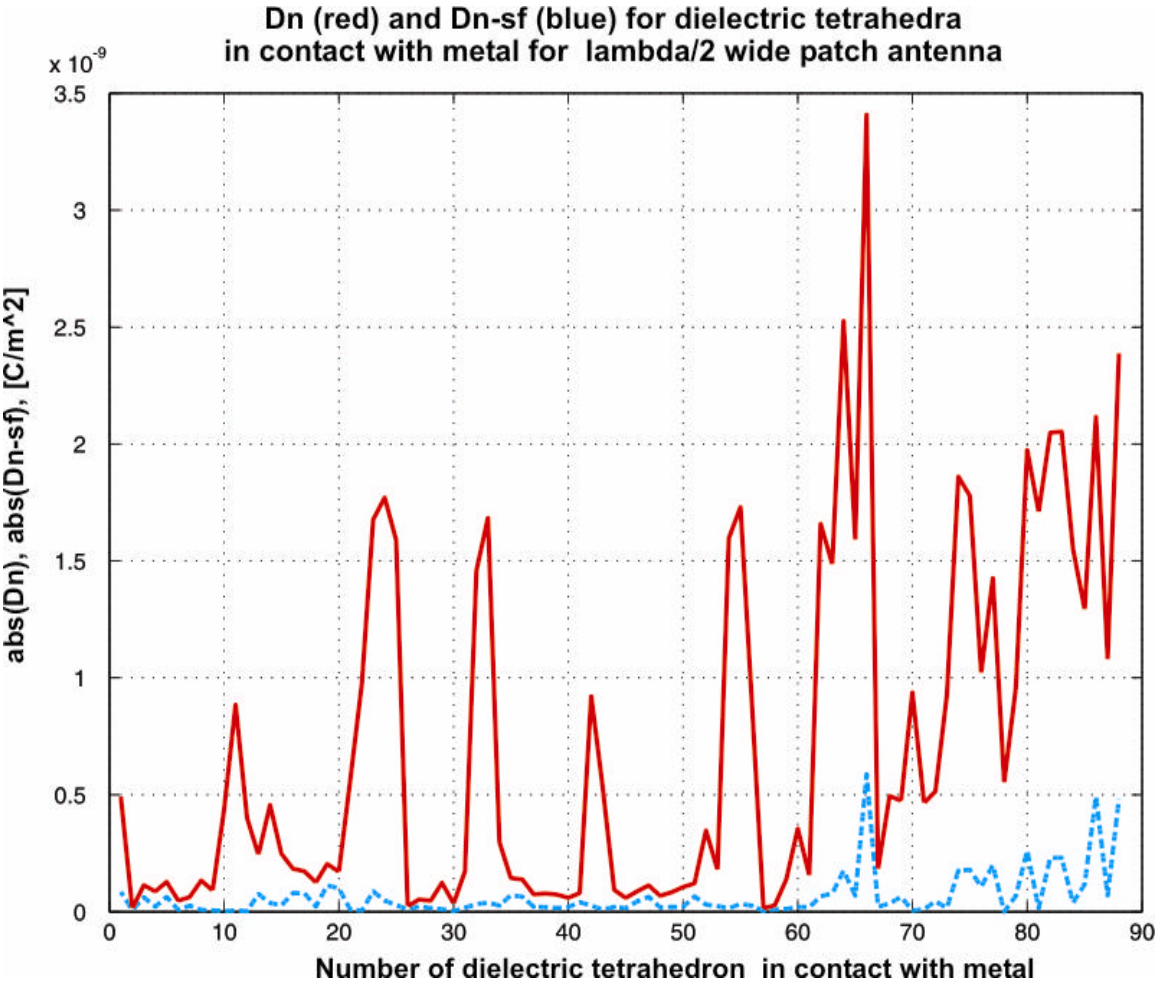

This issue was introduced as a point of concern in section 1.3.3-g and it was suggested that the boundary conditions could be explicitly implemented in the program to assure that they are accurately satisfied.

We tried to implement the boundary condition for the metal feed embedded in the dielectric volume. According to the definition of volume RWG basis functions, a basis function corresponding to a non-boundary face is defined in a pair of tetrahedra sharing that face, whereas for a boundary face, the basis function is defined only in a single tetrahedron. This gives rise to a possible air gap at the metal-dielectric interface as discussed in section 1.3. We tried to avoid this air gap adjacent to the feed.

In the surface-volume mesh, any triangular element of the metal feed surface is sandwiched between two dielectric tetrahedra. These two tetrahedra would belong to two different volume RWG basis functions according to the definition. To implement the boundary condition it is necessary to eliminate one of the variables from the equation,

$$D_n^+(K^+ - K^-) - s_S(\vec{r}) = 0$$

In the Matlab script this equation was implemented through a few matrix manipulations. Corresponding terms in the MoM impedance matrix are updated as well. Effectively, for avoiding the air gap, we considered that these two tetrahedra shared a single face (which also was a triangular element of the feed). The results were improved for all dielectric constants of the patch antenna substrate. Table A.1 shows the test results.

Table A.1 Test results for boundary conditions implemented only for feed

e_r	**Percent Error** Grid Size: 4x8 Feed division: 1, Patch border rendering: 0 Surface RWG elements: 117 Volume RWG elements: 590	**Percent Error** Grid Size: 4x8 Feed division: 1, Patch border rendering: 1 Surface RWG elements: 265 Volume RWG elements: 1092
2	3.89	3.21
3	5.05	4.40
5	6.93	6.20
10	7.17	6.54

Similarly, appropriate boundary conditions were implemented for the dielectric faces in contact with the metal patch. Table A.2 shows the test results.

Table A.2 Test results for boundary conditions implemented for all metal-dielectric interfaces

e_r	**Percent Error** Grid Size: 4x8 Feed division: 1, Patch border rendering: 0 Surface RWG elements: 117 Volume RWG elements: 590	**Percent Error** Grid Size: 4x8 Feed division: 1, Patch border rendering: 1 Surface RWG elements: 265 Volume RWG elements: 1092
2	1.22	2.01
3	1.96	2.53
5	1.89	2.31
10	3.33	3.33

Considerable improvement is observed in the performance of the solver after implementing the boundary conditions. The solver with boundary conditions was not as extensively tested as the original solver.

Appendix B

Gaussian formulae for triangular patches [12, 13]

Degree of Precision=1 Number of Points=1

Points	Triangular Coordinates	Weights
a	1/3, 1/3, 1/3	1

Degree of Precision=2 Number of Points=3

Points	Triangular Coordinates	Weights
a	1/2, 1/2, 0	1/3
b	0, 1/2, 1/2	1/3
c	1/2, 0, 1/2	1/3

Degree of Precision=3 Number of Points=4

Points	Triangular Coordinates	Weights
a	1/3, 1/3, 1/3	-27/48
b	0.6, 0.2, 0.2	25/48
c	0.2, 0.6, 0.2	25/48
d	0.2, 0.2, 0.6	25/48

Degree of Precision=4 Number of Points=7

Points	Triangular Coordinates	Weights
a	1/3, 1/3, 1/3	0.2250000000
b	a_1, ß$_1$, ß$_1$	0.1323941527
c	ß$_1$, a_1, ß$_1$	0.1323941527
d	ß$_1$, ß$_1$, a_1	0.1323941527
e	a_2, ß$_2$, ß$_2$	0.1259391805
f	ß$_2$, a_2, ß$_2$	0.1259391805
g	ß$_2$, ß$_2$, a_2	0.1259391805

With

a_1=0.0597158717

$ß_1$=0.4701420641
a_2=0.7974269853
$ß_2$=0.1012865073

Degree of Precision=7 Number of Points=13

Points	Triangular Coordinates	Weights
a	1/3, 1/3, 1/3	-0.149570044467670
b	a_1, $ß_1$, $ß_1$	0.175615257433204
c	$ß_1$, a_1, $ß_1$	0.175615257433204
d	$ß_1$, $ß_1$, a_1	0.175615257433204
e	a_2, $ß_2$, $ß_2$	0.053347235608839
f	$ß_2$, a_2, $ß_2$	0.053347235608839
g	$ß_2$, $ß_2$, a_2	0.053347235608839
h	a_3, $ß_3$, $?_3$	0.077113760890257
i	$?_3$, a_3, $ß_3$	0.077113760890257
j	$ß_3$, $?_3$, a_3	0.077113760890257
k	a_3, $?_3$, $ß_3$	0.077113760890257
l	$?_3$, $ß_3$, a_3	0.077113760890257
m	$ß_3$, a_3, $?_3$	0.077113760890257

with

a_1=0.479308067841923
$ß_1$=0.260345966079038
a_2=0.869739794195568
$ß_2$=0.065130102902216
a_3=0.638444188569809
$ß_3$=0.312865496004875
$?_3$=0.04869031542531

Analytical formulas for self-integrals over patches [14]

The integrals given below [14] are necessary to compute expressions (2.1.22) and (2.1.23) with the help of equations (2.1.24) and (2.1.25). Here,

$$a = (\vec{r}_3 - \vec{r}_1)\cdot(\vec{r}_3 - \vec{r}_1), b = (\vec{r}_3 - \vec{r}_1)\cdot(\vec{r}_3 - \vec{r}_2), c = (\vec{r}_3 - \vec{r}_2)\cdot(\vec{r}_3 - \vec{r}_2), \det = \sqrt{a - 2b + c} \qquad \text{(B1)}$$

and A is the area of the triangular patch. The remaining integrals are obtained using cyclic transformation.

$$\left(\frac{1}{4A^2}\right)\int_A\int_{A'}\frac{1}{|\vec{r}-\vec{r}'|}\,da\,da' = \left[\begin{array}{l} \dfrac{\log\left(\dfrac{\left(a-b+\sqrt{a}\det\right)\left(b+\sqrt{a}\sqrt{c}\right)}{\left(-b+\sqrt{a}\sqrt{c}\right)\left(-a+b+\sqrt{a}\det\right)}\right)}{6\sqrt{a}} + \\ \dfrac{\log\left(\dfrac{\left(b+\sqrt{a}\sqrt{c}\right)\left(-b+c+\sqrt{c}\det\right)}{\left(b-c+\sqrt{c}\det\right)\left(-b+\sqrt{a}\sqrt{c}\right)}\right)}{6\sqrt{c}} + \\ \dfrac{\log\left(\dfrac{\left(a-b+\sqrt{a}\det\right)\left(-b+c+\sqrt{c}\det\right)}{\left(b-c+\sqrt{c}\det\right)\left(-a+b+\sqrt{a}\det\right)}\right)}{6\det} \end{array}\right] \qquad \text{(B2)}$$

$$\left(\frac{1}{4A^2}\right)\iint_A\iint_{A'} l_1{}'\, l_1 \frac{1}{|\vec{r}-\vec{r}'|}\,dada' = \left[\begin{array}{l} \dfrac{\log\left(\dfrac{b+\sqrt{a}\sqrt{c}}{b-c+\sqrt{c}\det}\right)}{40\sqrt{c}} + \dfrac{\log\left(\dfrac{-b+c+\sqrt{c}\det}{-b+\sqrt{a}\sqrt{c}}\right)}{40\sqrt{c}} + \\ \dfrac{\left(\sqrt{a}\det-\sqrt{c}\det\right)}{120\det^3} + \dfrac{-\left(\sqrt{a}\sqrt{c}\right)+\sqrt{a}\det}{120a^{\frac{3}{2}}} + \\ \dfrac{(2a-5b+3c)\log\left(\dfrac{\left(a-b+\sqrt{a}\det\right)\left(c-b+\sqrt{c}\det\right)}{\left(b-a+\sqrt{a}\det\right)\left(b-c+\sqrt{c}\det\right)}\right)}{120\det^3} + \\ \dfrac{(2a+b)\log\left(\dfrac{\left(b+\sqrt{a}\sqrt{c}\right)\left(a-b+\sqrt{a}\det\right)}{\left(-b+\sqrt{a}\sqrt{c}\right)\left(-a+b+\sqrt{a}\det\right)}\right)}{120a^{\frac{3}{2}}} \end{array}\right] \quad \text{(B3)}$$

$$\left(\frac{1}{4A^2}\right)\iint_A\iint_{A'} l_2{}'\, l_1 \frac{1}{|\vec{r}-\vec{r}'|}\,dada' = \left[\begin{array}{l} \dfrac{\log\left(\dfrac{b+\sqrt{a}\sqrt{c}}{b-c+\sqrt{c}\det}\right)}{120\sqrt{c}} + \dfrac{\log\left(\dfrac{a-b+\sqrt{a}\det}{-b+\sqrt{a}\sqrt{c}}\right)}{120\sqrt{a}} + \\ \dfrac{(2a-3b+c)\log\left(\dfrac{a-b+\sqrt{a}\det}{b-c+\sqrt{c}\det}\right)}{120\det^3} + \\ \dfrac{(a-3b+2c)\log\left(\dfrac{-b+c+\sqrt{c}\det}{-a+b+\sqrt{a}\det}\right)}{120\det^3} + \\ \dfrac{-3\sqrt{a}+3\det}{120c} + \dfrac{-3\sqrt{c}+3\det}{120a} \\ + \dfrac{(3b+2c)\log\left(\dfrac{-b+c+\sqrt{c}\det}{-b+\sqrt{a}\sqrt{c}}\right)}{120c^{\frac{3}{2}}} + \\ + \dfrac{(2a+3b)\log\left(\dfrac{b+\sqrt{a}\sqrt{c}}{-a+b+\sqrt{a}\det}\right)}{120a^{\frac{3}{2}}} \end{array}\right] \quad \text{(B4)}$$

$$\left(\frac{1}{4A^2}\right)\iint_A\iint_{A'} l_1{}' \frac{1}{|\vec{r}-\vec{r}'|}\,da\,da' = \left[\begin{array}{l} \dfrac{-\log\left(\dfrac{-b+\sqrt{a}\sqrt{c}}{a-b+\sqrt{a}\det}\right)}{24\sqrt{a}} + \dfrac{\log\left(\dfrac{b+\sqrt{a}\sqrt{c}}{b-c+\sqrt{c}\det}\right)}{24\sqrt{c}} + \\ \dfrac{-\left(\sqrt{a}\sqrt{c}\right)+\left(\sqrt{a}\det\right)}{24a^{\frac{3}{2}}} + \dfrac{(a+b)\log\left(\dfrac{b+\sqrt{a}\sqrt{c}}{-a+b+\sqrt{a}\det}\right)}{24a^{\frac{3}{2}}} + \\ \dfrac{\log\left(\dfrac{a-b+\sqrt{a}\det}{b-c+\sqrt{c}\det}\right)}{24\det} + \dfrac{\log\left(\dfrac{-b+\sqrt{a}\sqrt{c}}{-b+c+\sqrt{c}\det}\right)}{12\sqrt{c}} + \\ \dfrac{\left(\sqrt{a}\det\right)-\left(\sqrt{c}\det\right)}{24\det^3} + \dfrac{(a-3b+2c)\log\left(\dfrac{-b+c+\sqrt{c}\det}{-a+b+\sqrt{a}\det}\right)}{24\det^3} \end{array}\right] \tag{B5}$$

Gaussian formulas for tetrahedral elements [13, 15]

Degree of Precision=1 Number of Points=1

Points	Tetrahedral Coordinates	Weights
A	1/4, 1/4, 1/4, 1/4	1

Degree of Precision=2 Number of Points=4

Points	Tetrahedral Coordinates	Weights
a	$\alpha, \beta, \beta, \beta$	1/4
b	$\beta, \alpha, \beta, \beta$	1/4
c	$\beta, \beta, \alpha, \beta$	1/4
d	$\beta, \beta, \beta, \alpha$	1/4

With

$\alpha = 0.58541020, \beta = 0.13819660$

Degree of Precision=3 Number of Points=5

Points	Tetrahedral Coordinates	Weights
A	1/4, 1/4, 1/4, 1/4	-4/5
B	$\alpha, \beta, \beta, \beta$	9/20
C	$\beta, \alpha, \beta, \beta$	9/20
D	$\beta, \beta, \alpha, \beta$	9/20
E	$\beta, \beta, \beta, \alpha$	9/20

With

$\alpha = 1/2, \beta = 1/6$

Degree of Precision=4 Number of Points=11

Points	Tetrahedral Coordinates	Weights
a	1/4, 1/4, 1/4, 1/4	-0.131555555555555550e-1
b	$\alpha_1, \beta_1, \beta_1, \beta_1$	0.762222222222222222e-2
c	$\beta_1, \alpha_1, \beta_1, \beta_1$	0.762222222222222222e-2
d	$\beta_1, \beta_1, \alpha_1, \beta_1$	0.762222222222222222e-2
e	$\beta_1, \beta_1, \beta_1, \alpha_1$	0.762222222222222222e-2
f	$\alpha_2, \alpha_2, \beta_2, \beta_2$	0.248888888888888888e-1
g	$\beta_2, \alpha_2, \alpha_2, \beta_2$	0.248888888888888888e-1
h	$\beta_2, \beta_2, \alpha_2, \alpha_2$	0.248888888888888888e-1
i	$\alpha_2, \beta_2, \beta_2, \alpha_2,$	0.248888888888888888e-1
j	$\beta_2, \alpha_2, \beta_2, \alpha_2,$	0.248888888888888888e-1
k	$\alpha_2, \beta_2, \alpha_2, \beta_2$	0.248888888888888888e-1

With

$\alpha_1 = 0.714285714285714285$
$\beta_1 = 0.785714285714285714$
$\alpha_2 = 0.399403576166799219$
$\beta_2 = 0.100596423833200785$

Appendix C

Mesh Generation

I. Plane Mesh:

1. Flow Chart for execution of wrapper.m.

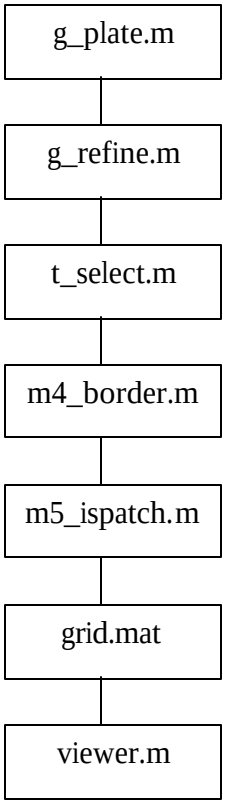

2. Explanation of individual functions:

`g_plate`

Creates uniform mesh for a plate (strip)

`Syntax:`

[p, t]=g_plate (W,H ,Nx, Ny, xf, yf, eps)

Description:

The function g_plate returns two matrices t and p, which correspond, to the vertices of the triangles and their x, y and z coordinates respectively for a given structure. The structure can be defined using the input parameters.

W = Ground plane width (along the x-axis)

H = Ground plane height (along the y-axis)

Nx = Mesh grid size in the x-direction

Ny = Mesh grid size in the y-direction

xf = Feed edges - x

yf = Feed edges -y

eps = Adjustment parameter for Delaunay triangulation

g_refine

Refines patch mesh close to patch/ground plane borders.

Syntax:

[p, t, PatchNumber]=g_refine (p, t, PatchNumber, IterP)

Description:

The function g_refine returns two matrices t and p which correspond to the vertices of the triangles and their x, y and z coordinates respectively for a given structure. It also returns PatchNumber which is row matrix of indices which specify the metal faces. The input

parameters to the function are the p and t matrices obtained from g_plate and IterP which specifies the order of patch border rendering.

t_select:

Selects certain triangular patches, to identify the patch or refine, using mouse.

Syntax:

[SelectNumber] = t_select (p, t)

Description:

The function t_select returns a row matrix corresponding to the triangular patches selected. The input parameters to the function are t and p, which correspond to the vertices of the triangles and their x, y, and z coordinates respectively for a given structure

m4_border:

Finds border triangles of the mesh and refines them.

Syntax:

[pn, tn]=m4_border (p, t, set, unset)

Description:

The function m4_border refines the patch border and returns two matrices tn and pn, which correspond, to the new vertices of the triangles and their x, y and z coordinates respectively

for a given structure. The structure to be refined can be described by the following input parameters.

set = Set of triangles that form the structure to be refined

unset = Set of triangles that do not have to be refined

t = vertices of the triangles of the original structure

p = x, y and z coordinates of the vertices of the original structure.

m5_ispatch:

Identifies the new set of patch triangles after mesh refinement.

Syntax:

[PatchNumberNew]=m5_ispatch (pn, tn, p, t, PatchNumber)

Description:

The function m5_ispatch identifies the new patch triangle after mesh refinement corresponding to tn and pn and returns a new value of patch number. The input parameters to the function are the old patch number along with the old values of p and t (before mesh refinement) and the values of p and t after mesh refinement, pn and tn.

viewer:

Viewer for the structure

Syntax:

viewer (p, t)

Description:

The function viewer is used to view the structure defined by p and t where t and p corresponds to the new vertices of the triangles and their x, y and z coordinates respectively for a given structure.

3. Data File

wrapper.m generates a data file called grid.mat. The parameters saved in this file are : H , PatchNumber , W , t , yf , Nx, Points , d , xc , Ny , R , eps , xf , Out , SelectNumber , p , yc

II. Volume Mesh:

1. Flow Chart for execution of wrapper.m

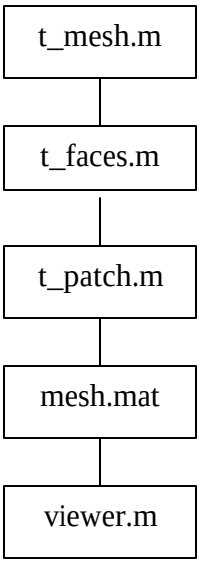

2. Explanation of individual functions:

`t_mesh:`

Creates volume tetrahedral mesh for the patch antenna using the given ground plane/patch mesh

`Syntax:`

[P, T]=t_mesh (p, R, xf, yf, h, Nf, eps, Interm)

`Description:`

The function t_mesh returns two matrices T and P which correspond to the vertices of the tetrahedron and their x, y and z coordinates respectively for a given structure. The structure can be defined using the input parameters.

h = Dielectric layer thickness (along the z-axis)

Nf = Feed subdivision number

Iterm = Layer subdivision number

eps = Adjustment (shift) parameter for Delaunay tessellation

xf = Feed edges - x

yf = Feed edges -y

R = Points to be cloned into the depth

t_faces:

Finds all faces and adjacent tetrahedra

Syntax:

[Faces, FacesBoundary, TetP, TetM]=t_faces (P, T)

Description:

The function t_faces returns all the inner and the boundary faces of the tetrahedra along with the indices of the plus and minus tetrahedra. The inputs to the function are the P and T

matrices, which correspond to the vertices of the tetrahedron and their x, y, and z coordinates respectively.

t_patch:

Recreates the mesh for the ground plane, patch, and feed using the tetrahedral faces.

Syntax:

[t, Faces, TetP, TetM, FeedFaces, MetalFaces, ContactFaces] = t_patch (p, P, t, Faces, FacesBoundary, TetP, TetM, PatchNumber, xf, yf, Nf, h, eps)

Description:

The function t_patch as an argument takes the variables that describe the mesh, and rearranges the arrays in a systematic manner. Faces in contact with the metal part of the structure i.e. patch, ground plane, feed are grouped separately, and faces completely inside the dielectric volume, faces on the boundary of the dielectric substrate are grouped separately as well. Same procedure is carried out for the plus and minus tetrahedrons. This saves considerable amount of computation in the later parts, since similar properties are associated with the different classes of dielectric faces. The variables that are returned can be described as:

Faces = All the faces in the structure (both metal and dielectric)

TetP = Plus tetrahedron

TetM = Minus Tetrahedron.

FeedFaces = Faces in contact with the feed.

MetalFaces = Faces in contact with patch, ground plane and feed

ContactFaces = Boundary faces.

viewer:

Visualizes the patch antenna structure.

Syntax:

viewer (p, t)

Description:

The function viewer is used to view the structure defined by p and t.

3. Data File

wrapper.m generates a data file called mesh.mat. The parameters saved in this file are: ContactFaces, MetalFaces, TetM, t, Faces, P, TetP, xf, FeedFaces, T, h, yf

III. Extracting parameters for RWG elements:

1. Flow Chart for execution of wrapper.m

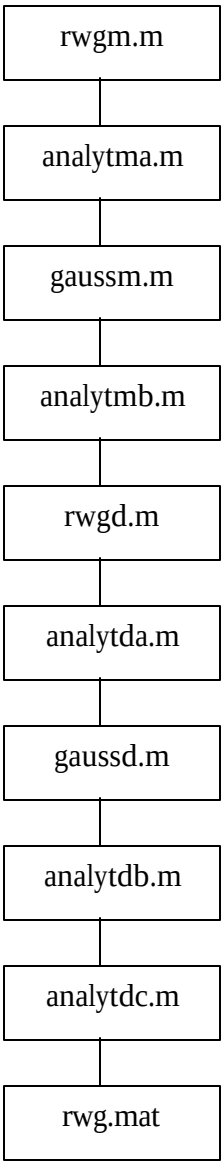

2. Explanation of individual functions:

`rwgm`

Computes parameters for metal triangles including self-integrals.

Syntax:

[geom] =rwgm (P, t, IndexF)

Description:

The function rwgm.m returns a structure geom which defines all the parameters of the metal triangles including self integrals. The self integrals for metal are calculated using the functions analytma.m and analytmb.m. The input parameters to the function are IndexF which defines the number of integration points and the P and t matrices which correspond to the vertices of the tetrahedrons and their x, y and z coordinates respectively for a given structure.

The structure geom includes the following parameters.

geom.PointsTotal	Integer	
geom.EdgesTotal	Integer	Total edges in the structure
geom.TrianglesTotal	Integer	Total triangles
geom. EdgeLength	[1,EdgesTotal]	Length of edge
geom.EdgeCenter	[3,EdgesTotal]	Coordinates of center
Geom.TriP	[1,EdgesTotal]	Index on plus triangle
geom.TriM_	[1,EdgesTotal]	Index on minus triangle
geom.VerP	[1,EdgesTotal]	Free vertex of plus triangle
geom.VerM	[1,EdgesTotal]	Free vertex of minus triangle
geom.AreaM	[1,TrianglesTotal]	Area of faces
geom.CenterM	[1,TrianglesTotal]	Center of metal faces
geom.IndexF	Integer	Order of integration for faces
geom.PointsF	[3,TrianglesTotal*IndexMI]	
geom.RHO	[3,3,TrianglesTotal*IndexMO]	Vector drawn from the free vertex to the center of the face

The integrals included in GEOM are listed in Table C.

analytma

Analytically calculated self integrals for metal face to metal face.

Syntax:

```
inline static void intsm (double *r1, double *r2, double
*r3, double *I1, double *I2, double *I3, double *I4);
```

Description:

The function analytma returns the numerically calculated metal to metal self integrals. The calculations are done using the formulae specified in appendix B.

gaussm

Locates the interior points on the face for Gaussian integration.

Syntax:

[Points, Weights]=gaussm (P, Index)

Description:

The function gaussm.m implements the Gaussian integration formulae given in appendix A. The outputs of the function are the integration points and their corresponding weights. The input to the function is the P matrix and a parameter Index whose value determines the integration formulae to be used.

analytmb

Numerically calculated self integrals for metal face to metal face.

Syntax:

[MM01, MM2, MM3]=analytmb (P)

Description:

The function analytmb returns the metal to metal self integrals geom.MM01, geom.MM2 and geom.MM3. The size and explanation of these matrices in given in the table above. The input to the function is the P matrix which corresponds to the x, y, and z coordinates of the vertices of the tetrahedron.

rwgd

Creates RWG's for dielectric and computes the parameters for separate tetrahedra including self-integrals.

Syntax:

[GEOM] = rwgd (P, T, t, CenterM, TetP, TetM, Faces, IndexF, IndexV, ContactFaces, MetalFaces)

Description:

The function rwgd.m returns a structure GEOM which defines all the parameters of the dielectric tetrahedron including self integrals. The self integrals for dielectric are calculated using the functions analytda.m, analytmb.m and analytdc.m. The input parameters to the function are IndexF and IndexV which defines the number of integration points for the face and volume respectively. The other input parameters are P and t matrices, which correspond to the vertices of the tetrahedrons and their x, y, and z coordinates respectively

for a given structure. Additional input parameters are CenterM, TetM, TetP, ContactFaces and MetalFaces which are calculated in volume mesh and saved in mesh. mat

The structure GEOM includes the following parameters

GEOM.TetrahedraTotal	integer	Total number of tetrahedrons in the structure
GEOM.FacesTotal	integer	Total number of Faces
GEOM.VolumeD	[1x204 double]	Volume of each tetrahedron
GEOM.TetP	[1x502 double]	Index on plus tetrahedron
GEOM.TetM	[1x502 double]	Index on plus tetrahedron
GEOM.VerDP	[1x502 double]	Free vertex of plus tetrahedron
GEOM.VerDM	[1x502 double]	Free vertex of minus tetrahedron
GEOM.AreaF	[1x502 double]	Area of face
GEOM.CenterF	[3x502 double]	Center of dielectric faces
GEOM.TriFace	[1x502 double]	triangle number for a given face
GEOM.FaceFac	{1x502 cell}	face number for a given face
GEOM.IndexV	integer	Order of Gaussian integration for volume
GEOM.PointsV	[3x1020 double]	
GEOM.Rho	[4x3x1020 double]	Vector drawn from the free vertex to the center of the tetrahedron.

The integrals included in GEOM are listed in Table C.

`analytda`

Computes self integrals from tetrahedron (volume) to tetrahedron (volume).

`Syntax:`

[D0, DD00, DD01, DD1, DD2, DD3]= analytda (P)

`Description`:

The function analytda returns matrices of numerically and analytically calculated volume to volume self integrals D0, DD00, DD01, DD1, DD2, and DD3. The size and explanation of these matrices in given in the table B1. The input to the function is the P matrix which corresponds to the x, y, and z coordinates of the vertices of the tetrahedron.

gaussd

Locates the interior points inside the dielectric volume for Gaussian integration.

Syntax:

[Points, Weights]=gaussd (P, Index)

Description:

The function gaussd.m implements the Gaussian integration formulae given in appendix B. The outputs of the function are the integration points and their corresponding weights. The input to the function is the P matrix and a parameter Index whose value determines the integration formulae to be used.

analytdb

Computes self integrals from dielectric faces (surface) to tetrahedron (volume).

Syntax:

[FD0P, FD1P, FD0M, FD1M] = analytdb (Vertexes, VP, VM)

Description:

The function analytdb returns matrices of numerically and analytically calculated surface to volume self integrals FD0P, FD1P, FD0M and FD1M. The size and explanation of these matrices in given in Table C. The input to the function is the P matrix which corresponds to the x, y, and z coordinates of the vertices of the tetrahedron.

analytdc

Computes self integrals from the metal face (surface) to dielectric tetrahedron (volume).

Syntax:

[MD1, MD2, MD3]=analytdc (Vertexes, VP)

Description:

The function analytdb returns matrices of numerically calculated metal surface to dielectric volume self integrals MD1, MD2 and MD3. The size and explanation of these matrices in given in the Table C. The inputs to the function are the Vertexes matrix which corresponds to the x, y, and z coordinates of the vertices of the tetrahedron and VP matrix which are the coordinates of the indices of the vertices of the plus tetrahedron.

3. Data File

wrapper.m generates a data file called rwg.mat. The parameters saved in this file are: ContactFaces, IndexF, T, h, Faces, IndexV, TetM, t, FeedFaces, MetalFaces, TetP, xf, P, yf and the structures geom and GEOM.

Table C

Self-integrals – metal structure

Obtained for the expansion

$$\frac{e^{-jkr}}{r} \approx \frac{1}{r} - jk - \frac{k^2 r}{2}$$

Script/ Function	Variable	Description	Size	Structure
rwgm analytma.m	MM00(m) Analytical	$\iint_{FF} \frac{1}{\lvert\vec{r}-\vec{r}'\rvert} d\vec{r}\,d\vec{r}'$ electric potential; from metal face to metal face	[TrianglesTotal]	geom
rwgm analytmb.m	MM01(m) Numerical	$\iint_{FF} \lvert\vec{r}-\vec{r}'\rvert d\vec{r}\,d\vec{r}'$ electric potential; from metal face to metal face	[TrianglesTotal]	geom
rwgm analytma.m	MM1(3,3,m) Analytical	$\iint_{FF} \frac{\vec{r}_i \cdot \vec{r}'_j}{\lvert\vec{r}-\vec{r}'\rvert} d\vec{r}\,d\vec{r}'$ magnetic vector potential; from metal face to metal face	[3,3, TrianglesTotal]	geom
rwgm analytmb.m	MM2(3,3,m) Numerical	$\iint_{FF} \vec{r}_i \cdot \vec{r}'_j d\vec{r}\,d\vec{r}'$ magnetic vector potential; from metal face to metal face	[3,3, TrianglesTotal]	geom
rwgm analytmb.m	MM3(3,3,m) Numerical	$\iint_{FF} \lvert\vec{r}-\vec{r}'\rvert \vec{r}_i \cdot \vec{r}'_j d\vec{r}\,d\vec{r}'$ magnetic vector potential; from metal face to metal face	[3,3, TrianglesTotal]	Geom.

Self-integrals – dielectric structure

Obtained for the expansion

$$\frac{e^{-jkr}}{r} \approx \frac{1}{r} - jk - \frac{k^2 r}{2}$$

Script/ Function	Variable	Description	Size	Structure
rwgd analytda.m	D0(3,3,m) Analytical	$\int_V \vec{r}_i \cdot \vec{r}_j d\vec{r}$ D/e term	[4,4,TetrahedraTotal]	GEOM
rwgd analytda.m	DD00(m) Numerical	$\iint_{VV} \frac{1}{\lvert\vec{r}-\vec{r}'\rvert} d\vec{r}\,d\vec{r}'$ electric potential; from tetrahedron to tetrahedron	[TetrahedraTotal]	GEOM
rwgd analytda.m	DD01(m) Numerical	$\iint_{VV} \lvert\vec{r}-\vec{r}'\rvert d\vec{r}\,d\vec{r}'$ electric potential; from tetrahedron to tetrahedron	[TetrahedraTotal]	GEOM
rwgd analytda.m	DD1(4,4,m) Numerical	$\iint_{VV} \frac{\vec{r}_i \cdot \vec{r}'_j}{\lvert\vec{r}-\vec{r}'\rvert} d\vec{r}\,d\vec{r}'$ magnetic vector potential; from tetrahedron to tetrahedron	[4,4,TetrahedraTotal]	GEOM
rwgd analytda.m	DD2(4,4,m) Numerical	$\iint_{VV} \vec{r}_i \cdot \vec{r}'_j d\vec{r}\,d\vec{r}'$ magnetic vector potential; from tetrahedron to tetrahedron	[4,4,TetrahedraTotal]	GEOM
rwgd analytda.m	DD3(4,4,m) Numerical	$\iint_{VV} \lvert\vec{r}-\vec{r}'\rvert \vec{r}_i \cdot \vec{r}'_j d\vec{r}\,d\vec{r}'$ magnetic vector potential; from tetrahedron to tetrahedron	[4,4,TetrahedraTotal]	GEOM

rwgd analytma.m	FF00(m) Analytical	$\iint_{FF} \frac{1}{\lvert\vec{r}-\vec{r}'\rvert} d\vec{r}\, d\vec{r}'$ electric potential; from face to face	[ContactFaces]	GEOM
rwgd analytmb.m	FF01(m) Numerical	$\iint_{FF} \lvert\vec{r}-\vec{r}'\rvert d\vec{r} d\vec{r}'$ electric potential; from face to face	[ContactFaces]	GEOM
rwgd analytdb.m	FD0P(m) Numerical	$\iint_{VF} \frac{1}{\lvert\vec{r}-\vec{r}'\rvert} d\vec{r}\, d\vec{r}'$ electric potential; from face to T^+ tetrahedron	[ContactFaces]	GEOM
rwgd analytdb.m	FD1P(m) Numerical	$\iint_{VF} \lvert\vec{r}-\vec{r}'\rvert d\vec{r} d\vec{r}'$ electric potential; from face to T^+ tetrahedron	[ContactFaces]	GEOM
rwgd analytdb.m	FD0M(m) Numerical	$\iint_{VF} \frac{1}{\lvert\vec{r}-\vec{r}'\rvert} d\vec{r}\, d\vec{r}'$ electric potential; from face to T^- tetrahedron	[ContactFaces]	GEOM
rwgd analytdb.m	FD1M(m) Numerical	$\iint_{VF} \lvert\vec{r}-\vec{r}'\rvert d\vec{r} d\vec{r}'$ electric potential; from face to T^- tetrahedron	[ContactFaces]	GEOM

Self-integrals – combined metal/dielectric structure

Obtained for the expansion

$$\frac{e^{-jkr}}{r} \approx \frac{1}{r} - jk - \frac{k^2 r}{2}$$

Script/Function	Variable	Description	Size	Structure
rwgd analytdc.m	MD1(4,4,m) Numerical	$\iint_{VF} \frac{\vec{r}_i \cdot \vec{r}'_j}{\lvert\vec{r} - \vec{r}'\rvert} d\vec{r} d\vec{r}'$ magnetic vector potential; from metal face to adjacent tetrahedron	[4,3,MetalFaces]	GEOM
rwgd analytdc.m	MD2(4,4,m) Numerical	$\iint_{VV} \vec{r}_i \cdot \vec{r}'_j d\vec{r} d\vec{r}'$ magnetic vector potential; from metal face to adjacent tetrahedron	[4,3,MetalFaces]	GEOM
rwgd analytdc.m	MD3(4,4,m) Numerical	$\iint_{VV} \lvert\vec{r} - \vec{r}'\rvert \vec{r}_i \cdot \vec{r}'_j d\vec{r} d\vec{r}'$ magnetic vector potential; from tetrahedron to tetrahedron	[4,3,MetalFaces]	GEOM

Appendix D

Method of Moments

1. Flow Chart for execution of wrapper.m

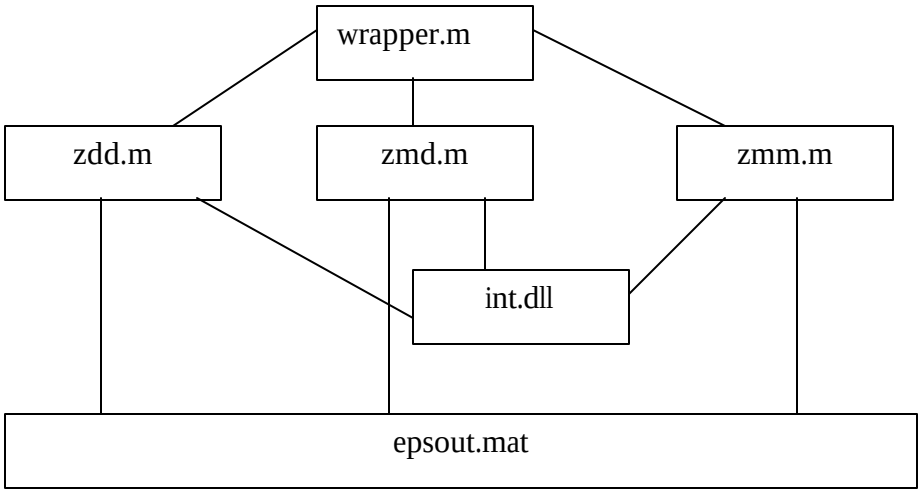

2. Explanation of individual functions:

`zmm`

Calculates the impedance matrix and the charge matrix corresponding to pure metal.

`Syntax:`

[ZMM, C] = zmm (geom, const, frequency, Array)

`Description:`

The function zmm returns matrices ZMM (Edgestotal by Edgestotal) and C which correspond to the impedance matrix for pure metal and the charge matrix (gives charge for metal faces in Array).The inputs to the function are two structures geom and const and the frequency of operation. The structure geom defines all the parameters of the metal triangles

including self integrals while the structure const defines the electromagnetic constants such as mu, epsilon, speed of light etc.

zdd

Calculates the impedance matrix corresponding to pure dielectric.

Syntax:

[ZDD, FD, FF] =zdd (GEOM, const, frequency, ContactFaces)

Description:

The function zdd returns matrices ZDD (FacesTotal by FacesTotal), FD and FF which correspond to the impedance matrix for pure dielectric, integrals from dielectric to face and self integrals from face to face. The inputs to the function are two structures GEOM and const and the frequency of operation along with ContactFaces. The structure GEOM defines all the parameters of the dielectric tetrahedron including self integrals while the structure const defines the electromagnetic constants such as mu, epsilon, speed of light etc.

zmd

Calculates the impedance matrix corresponding to metal dielectric interaction.

Syntax:

[ZMD] =zmd (GEOM, geom, const, frequency, ContactFaces, FV, FD, FF)

Description:

The function zmd returns matrix ZMD (FacesTotal by EdgesTotal), which correspond to the impedance matrix for metal dielectric interaction. The inputs to the function are three structures geom, GEOM and const and the frequency of operation along with ContactFaces and integrals FV, FD and FF. The structure GEOM defines all the parameters of the dielectric tetrahedron including self integrals while geom defines all the parameters of the metal triangles including self integrals and the structure const defines the electromagnetic constants such as mu, epsilon, speed of light etc. The integrals FD and FF are calculated in zdd and are used directly.

`int`

Calculates the integrals for computation of impedance matrix.

`Input Parameters:`

Points = number of integration points for triangle or tetrahedron.

weights = the weights of the individual 'Points'.

RHO = vector from the free vertex all the 'Points' on the triangle or tetrahedron

subpoints = total number of integration points in each triangle or tetrahedron.

elems = number of triangles or tetrahedrons.

vertexes = 3 for a triangle and 4 for tetrahedron.

minusK_r, minusK_i = real and imaginary part of k (wave number)

3. Data File

wrapper.m generates a data file called epsout.mat. The parameters saved in this file are:

FEEDPOWER, FREQUENCY, IMPEDANCE .